



## 저작자표시-비영리-변경금지 2.0 대한민국

이용자는 아래의 조건을 따르는 경우에 한하여 자유롭게

- 이 저작물을 복제, 배포, 전송, 전시, 공연 및 방송할 수 있습니다.

다음과 같은 조건을 따라야 합니다:



저작자표시. 귀하는 원저작자를 표시하여야 합니다.



비영리. 귀하는 이 저작물을 영리 목적으로 이용할 수 없습니다.



변경금지. 귀하는 이 저작물을 개작, 변형 또는 가공할 수 없습니다.

- 귀하는, 이 저작물의 재이용이나 배포의 경우, 이 저작물에 적용된 이용허락조건을 명확하게 나타내어야 합니다.
- 저작권자로부터 별도의 허가를 받으면 이러한 조건들은 적용되지 않습니다.

저작권법에 따른 이용자의 권리는 위의 내용에 의하여 영향을 받지 않습니다.

이것은 [이용허락규약\(Legal Code\)](#)을 이해하기 쉽게 요약한 것입니다.

[Disclaimer](#)

이학박사 학위논문

**Vertical feedback mechanism of  
winter Arctic amplification and its  
relative role to horizontal process**

**- Focusing on the Barents & Kara Seas -**

겨울철 북극 증폭에 관한 수직 되먹임 기작과  
수평과정과의 상대적 역할  
- 바렌츠 카라해를 중심으로 -

2019 년 8 월

서울대학교 대학원

지구환경과학부

김 지 영

# **Vertical feedback mechanism of winter Arctic amplification and its relative role to horizontal process**

**- Focusing on the Barents & Kara Seas -**

겨울철 북극 증폭에 관한 수직 되먹임 기작과  
수평과정과의 상대적 역할: 바렌츠 카라해를 중심으로

지도 교수 Kwang-Yul Kim

이 논문을 이학박사 학위논문으로 제출함

2019 년 6 월

서울대학교 대학원

지구환경과학부

김 지 영

김지영의 이학박사 학위논문을 인준함

2019 년 7 월

위 원 장 \_\_\_\_\_ (인)

부위원장 \_\_\_\_\_ (인)

위 원 \_\_\_\_\_ (인)

위 원 \_\_\_\_\_ (인)

위 원 \_\_\_\_\_ (인)

# **Abstract**

## **Vertical feedback mechanism of winter Arctic amplification and its relative role to horizontal process - Focusing on the Barents & Kara Seas -**

Ji-Young Kim

School of Earth and Environmental Sciences

The Graduate School

Seoul National University

Sea ice reduction is accelerating in the Barents and Kara Seas. Several mechanisms are proposed to explain the accelerated loss of Arctic sea ice, which remains to be controversial. In the present study, detailed physical mechanism of sea ice reduction in winter (December–February) is identified from the daily ERA interim reanalysis data. Downward longwave radiation is an essential element for sea ice reduction, but can primarily be sustained by excessive upward heat flux from the sea surface exposed to air in the region of sea ice loss. The increased turbulent heat flux is used to increase air temperature and specific humidity in the lower troposphere, which in turn increases downward longwave radiation. This feedback process is clearly observed in the Barents and Kara Seas in the reanalysis data. A quantitative assessment reveals that this feedback process is being amplified at the rate of  $\sim 8.9\%$  every year during 1979–2018. Availability of excessive heat flux is necessary for the maintenance of this feedback process; a similar mechanism of sea ice loss is expected to take



place over the sea-ice covered polar region, when sea ice is not fully recovered in winter.

Moreover, relative role of vertical processes resulting from the reduction of sea ice in the Barents-Kara Seas is not clearly understood in comparison with the horizontal heat and moisture advection. Moisture, thermal energy and moist static energy budgets are analyzed over the region of sea ice reduction in order to delineate the relative roles of horizontal and vertical processes. A detailed analysis of energy and moisture budgets in the atmospheric column indicates that both the vertical source from the release of heat flux and moisture due to sea ice reduction and the horizontal advection of heat and moisture are essential for explaining the variation of temperature and specific humidity over the Barents-Kara Seas. The vertical flux term explains a slightly larger fraction of the mean increase in temperature and specific humidity, while the horizontal advection is a major source of variability in temperature and specific humidity in the atmospheric column.

**Keywords:** Arctic amplification, feedback mechanism, vertical & horizontal processes, Barents and Kara Seas, CSEOF

**Student Number:** 2012-30893

# Table of contents

<b>Abstract.....</b>	<b>i</b>
<b>Table of contents.....</b>	<b>iii</b>
<b>List of tables .....</b>	<b>v</b>
<b>List of figures.....</b>	<b>vi</b>
<b>Chapter 1. Introduction .....</b>	<b>1</b>
1.1. Background.....	1
1.2. Objectives.....	5
<b>Chapter 2. Data and Methodology .....</b>	<b>7</b>
2.1. Data .....	7
2.2. Methodology.....	7
<b>Chapter 3. Vertical Feedback Mechanism of Winter Arctic Amplification and Sea Ice Loss.....</b>	<b>10</b>
3.1. CSEOF mode of Arctic amplification and sea ice loss.....	10
3.2. Sensitivity test on the choice of datasets .....	22
3.3. Vertical feedback mechanism.....	28
<b>Chapter 4. Relative Roles of Horizontal and Vertical Processes in the Physical Mechanism of Winter Arctic Amplification .....</b>	<b>38</b>
4.1. Moisture budget.....	42
4.2. Thermal energy budget .....	48
4.3. Moist static energy budget.....	58
4.4. Sensitivity test on the level of closure .....	65
<b>Chapter 5. Concluding Remarks .....</b>	<b>72</b>

<b>References.....</b>	<b>76</b>
<b>국문초록 .....</b>	<b>83</b>

# List of tables

**Table 4.1.** Statistics of the lower tropospheric (1000–850 hPa) winter moisture budget averaged over the region of sea ice reduction (21°–79.5°E, 75°–79.5°N) in the Barents-Kara Seas: SH is specific humidity, H ADV is horizontal advection of moisture, SRC is source (evaporation minus precipitation), V CNV is vertical convection, TOT is sum of advection, source and convection terms, and ERR is the difference between specific humidity and TOT. .... 47

**Table 4.2.** Statistics of the lower tropospheric (1000–850 hPa) winter heat budget averaged over the region of sea ice reduction (21°–79.5°E, 75°–79.5°N) in the Barents-Kara Seas: AIR T is atmospheric temperature, H ADV is horizontal advection of heat, FLX is turbulent heat flux, RAD is greenhouse effect, V CNV is vertical convection, TOT is sum of all contributions, and ERR is the difference between air temperature and TOT. .... 57

# List of figures

**Figure 3.1.** (a) The yearly trend (%) of winter sea ice reduction in the Arctic Ocean during 1979–2018, (b) the winter (Dec. 1–Feb. 28) averaged loading vector of the sea ice loss mode, (c) the corresponding PC (amplitude) time series (*red solid curve*) and amplification curve (*blue dashed curve*), and (d) actual sea ice concentration in the sea-ice loss region ( $21^{\circ}$ – $79.5^{\circ}$  E  $\times$   $75^{\circ}$ – $79.5^{\circ}$  N; the boxed area in (a) and (b)) of the Barents and Kara Seas (*black dotted curve*), sea ice concentration according to the sea ice loss mode (*red curve*) and a projection (*blue dashed curve*) based on the exponential fit of the amplitude time series in (c). ..... 13

**Figure 3.2.** (a) The decadal trend ( $^{\circ}$ C) of winter 2 m air temperature increase in the Arctic Ocean during 1979–2016, (b) the winter averaged loading vector of regressed 2 m air temperature in the sea ice loss mode, (c) 30 days moving averaged winter 2 m air temperature variations in the sea-ice loss region ( $21^{\circ}$ – $79.5^{\circ}$  E  $\times$   $75^{\circ}$ – $79.5^{\circ}$  N; the boxed area in (a) and (b)) of the Barents and Kara Seas; actual variation from the raw data (*black dotted curve*), reconstructed variation according to the sea ice loss mode (*red curve*). The green contours in (a)–(b) represent sea ice reduction in Fig. 3.1(b) (the same hereinafter). ..... 14

**Figure 3.3.** Winter averaged patterns of sea ice loss mode: (a) sea ice (*shading*) and 2 m air temperature (*contour*), (b) 1000–850 hPa specific humidity, (c) upward longwave radiation, (d) downward longwave radiation, (e) turbulent (sensible + latent) heat flux, (f) 850 hPa air temperature. The numbers in parenthesis are contour intervals and negative contours are dashed..... 15

**Figure 3.4.** Anomalous daily sea ice concentration (*blue curve*) and upward longwave radiation (*red curve*) averaged over the region of sea ice loss ( $21^{\circ}$ – $79.5^{\circ}$  E  $\times$   $75^{\circ}$ – $79.5^{\circ}$  N) with respective mean values (*straight lines*). Winter days are counted from December 1. .... 16

**Figure 3.5.** Winter-averaged patterns of anomalous atmospheric condition: (a) 2 m air temperature, contour interval is in parenthesis, (b) lower tropospheric (1000–900 hPa) geopotential height (*red contour*) and wind (*black arrow line*), sea ice reduction (%), (*shading*), (c) vertical cross section along  $60^{\circ}$  E of lower tropospheric (1000–850 hPa) air temperature, geopotential height and wind, and (d) along  $80^{\circ}$  N. Temperature is in shading (0.4 K), geopotential height is in black contours (3 m), and (c) zonal and (d)

meridional winds are in blue contours ( $0.2 \text{ m s}^{-1}$ ). (e and f) pressure layer thickness ( $\Delta Z = Z(p_1) - Z(p_0)$ ) derived from the geopotential height pattern in (c) and (d) (*shading*) and that derived from the hydrostatic equation (*contour*). The red contour represents the thickness of 1.5 m. The level  $p_1$  is the level used for plotting and  $p_0$  is the pressure level below  $p_1$  at the interval of 25 hPa..... 20

**Figure 3.6.** Winter-averaged patterns of (a) 850 hPa air temperature (*shading*) and 2 m air temperature (*contour*), (b) 900 hPa specific humidity (*shade*) and downward longwave radiation at surface (*contour*), (c) net (upward minus downward) longwave radiation at surface (*shade*) and SAT (*contour*), and (d) total cloud liquid water (*shading*) and total cloud ice water (*contour*) for the sea ice loss mode. The red contour is drawn at the value of the contour interval. .... 21

**Figure 3.7.** The regressed patterns of atmospheric variables based on the NCEP reanalysis product (1979-2016). The target is the sea ice loss mode. .... 24

**Figure 3.8.** The regressed patterns of atmospheric variables based on the MERRA reanalysis product (1979-2015). The target is the sea ice loss mode. .... 25

**Figure 3.9.** The regressed patterns of atmospheric variables based on the JRA-55 reanalysis product (1979-2017). The target is the sea ice loss mode..... 26

**Figure 3.10.** The winter (DJF) (a) total precipitation (mm) and (b) evaporation (mm) for the sea ice loss mode based on the ERA-Interim reanalysis product, (c) total precipitation (mm) and (d) evaporation (mm) based on the MERRA reanalysis product (1979-2015). .... 27

**Figure 3.11.** Winter average pattern of sea ice loss mode in the Barents and Kara Seas: (a) sea ice reduction (%), (*shading*), 2 m air temperature (*red contour*) and 850 hPa temperature (*black contour*), (b) upward longwave radiation (*red contour*) and downward longwave radiation (*black contour*), (c) sensible heat flux (*red contour*) and latent heat flux (*black contour*), and (d) net energy balance (sensible heat flux + latent heat flux + upward longwave radiation – downward longwave radiation)..... 31

**Figure 3.12.** Daily patterns of variability over the region of sea ice loss ( $21^\circ - 79.5^\circ \text{ E} \times 75^\circ - 79.5^\circ \text{ N}$ ): (a) upward longwave radiation (*blue dashed*), downward longwave radiation (*blue dotted*), net longwave radiation (*blue*

*solid*) with its mean value (*blue straight line*), sensible heat flux (*red dashed*), latent heat flux (*red dotted*), and turbulent heat flux (*red solid*) with its mean value (*red straight line*), (b) 2 m air temperature (*red*), 850 hPa air temperature  $\times 2$  (*black*), and upward longwave radiation (*blue*), and (c) same as (b) except for the regressed downward longwave radiation (*blue*). The straight lines in (b) and (c) represent the winter mean value of anomalous 2 m air temperature. Correlation of upward and downward longwave radiation with 2 m air temperature is respectively 0.88 and 0.91, whereas with 850 hPa air temperature is 0.66 and 0.85. .... 32

**Figure 3.13.** Periodogram of upward longwave radiation (*blue dashed*), downward longwave radiation (*blue*), 2 m air temperature (*red dashed*) and 850 hPa air temperature (*red*). .... 33

**Figure 3.14.** Lagged correlations: (a) correlation of upward (*solid lines*) and downward (*dotted lines*) longwave radiations with 2 m air temperature (*blue*), 850 hPa temperature (*red*), and sea ice concentration (*black*), and (b) a blowup of the boxed region in (a). Longwave radiation lags the other variable for a positive lag. Lagged correlation between 2 m air temperature and 850 hPa air temperature (*black dashed line*); 2 m air temperature leads 850 hPa temperature for a positive lag. .... 34

**Figure 3.15.** A proposed feedback mechanism of Arctic amplification. Increased net upward energy flux increases air temperature. As a result, downward longwave radiation increases, which results in sea ice reduction. This loop seems to amplify by  $\sim 8.9\%$  annually. .... 37

**Figure 4.1.** (a and b) The vertical pattern of winter-averaged (temperature (*shading*), geopotential (*black contour*;  $3\text{ m}^2\text{ s}^2$ ) and wind (*green contour*;  $0.2\text{ m s}^{-1}$ ), and (c and d) specific humidity (*shading*) and saturation specific humidity (*contour*;  $0.05\text{ g kg}^{-1}$ ) along  $60^\circ\text{E}$  and  $80^\circ\text{N}$ . The blue contour in the upper panel is at  $12\text{ m}^2\text{ s}^2$ . The red contour in the lower panel is at  $0.2\text{ g kg}^{-1}$ . .... 40

**Figure 4.2.** Winter-averaged (a) moisture transport (*streamline*) and its convergence (*shading*), and (b) heat transport (*streamline*) and its convergence (*shading*) in the lower troposphere (1000–850 hPa) associated with the sea ice loss mode. The green contours represent the reduction of sea ice concentration. .... 41

**Figure 4.3.** The winter-averaged lower tropospheric (1000–850 hPa) patterns of variables: (a) specific humidity, (b) moisture advection, (c) moisture

source (evaporation minus precipitation), and (d) total (horizontal plus vertical) moisture supply. All the terms are converted into specific humidity ( $\text{g kg}^{-1}$ ).....	45
<b>Figure 4.4.</b> (a) Daily fluctuation of 1000–850 hPa averaged specific humidity (SH), evaporation minus precipitation (SRC), and horizontal moisture transport (ADV) averaged over the region of sea ice reduction ( $21^{\circ}$ – $79.5^{\circ}\text{E}$ , $75^{\circ}$ – $79.5^{\circ}\text{N}$ ) in the Barents-Kara Seas (boxed area in Fig. 3.1a). The straight lines represent the winter means of individual variables. (b) Lagged correlation between specific humidity and horizontal moisture transport ( <i>blue</i> ), between the horizontal transport and source (evaporation minus precipitation) ( <i>black</i> ), and between the specific humidity and the total (source plus advection) ( <i>red</i> ). .....	46
<b>Figure 4.5.</b> (a) The winter-averaged spatial pattern of the greenhouse effect ( $\text{W m}^{-2}$ ). (b) The daily variation of specific humidity ( <i>red</i> ) in the lower troposphere (1000–850 hPa) and the greenhouse effect ( <i>blue</i> ) averaged over the region of sea ice reduction ( $21^{\circ}$ – $79.5^{\circ}\text{E} \times 75^{\circ}$ – $79.5^{\circ}\text{N}$ ) in the Barents-Kara Seas. ....	52
<b>Figure 4.6.</b> The vertical profile of anomalous temperature and specific humidity over the region of sea ice reduction ( $21^{\circ}$ – $79.5^{\circ}\text{E} \times 75^{\circ}$ – $79.5^{\circ}\text{N}$ ) in the Barents-Kara Seas.....	53
<b>Figure 4.7.</b> The winter-averaged lower-tropospheric (1000–850 hPa) patterns of (a) total heat, (b) heat transport, (c) turbulent (sensible + latent) heat flux, and (d) greenhouse effect. All the terms are converted into temperature anomalies (K). .....	54
<b>Figure 4.8.</b> The winter averaged lower tropospheric (1000–850 hPa) patterns of (a) total heating converted into temperature, and (b) atmospheric temperature. ....	55
<b>Figure 4.9.</b> (a) Daily fluctuation of 1000–850 hPa averaged temperature (AIR T), turbulent flux (FLX), radiation (RAD), and horizontal heat transport (ADV). The thick red curve is the sum of turbulent flux and radiation (SRC). The straight lines represent the winter means of individual variables. (b) Lagged correlation between temperature and horizontal transport ( <i>blue</i> ), between the horizontal transport and the other source terms ( <i>black</i> ), and between the temperature and the total energy ( <i>red</i> ). .....	56



- Figure 4.10.** The winter-averaged regressed pattern of moist static energy (*contours*) at (a) 1000 hPa and (b) 850 hPa on top of sea ice anomaly pattern (*shading*)..... 61
- Figure 4.11.** Winter-averaged pattern of 1000–850 hPa daily (a) advection, (b) flux, (c) radiation, and (d) total (right-hand side of (27)). All quantities are scaled by  $c_p(p_0 - p)$ . ..... 62
- Figure 4.12.** Winter-averaged pattern of 1000–850 hPa daily (a) moist static energy and (b) total heating term (right-hand side of (27)). All quantities are scaled by  $c_p(p_0 - p)$ . ..... 63
- Figure 4.13.** (a) Daily fluctuation of 1000–850 hPa averaged moist static energy (MSE), turbulent flux (FLX), radiation (RAD), horizontal advection of moist static energy (ADV), and sum of all contributions (TOT). The straight lines represent the winter means of individual variables. (b) Lagged correlation between moist static energy (*m*) and horizontal advection (*blue*) and total heating term (*red*), and between horizontal advection and flux (*black*)..... 64
- Figure 4.14.** The winter-averaged lower tropospheric (1000–900 hPa) patterns of variables: (a) specific humidity, (b) moisture transport, (c) moisture source (evaporation – precipitation), and (d) total (horizontal plus vertical) moisture source. All the source terms are converted into specific humidity ( $\text{g kg}^{-1}$ ). (e) Daily fluctuation of 1000–900 hPa averaged specific humidity (SH), evaporation minus precipitation (SRC), and horizontal moisture transport (ADV) averaged over the region of sea ice reduction ( $21^\circ\text{--}79.5^\circ\text{E}$ ,  $75^\circ\text{--}79.5^\circ\text{N}$ ) in the Barents-Kara Seas (boxed area in Fig. 3.1a). The straight lines represent the winter means of individual variables..... 66
- Figure 4.15.** The winter-averaged lower tropospheric (1000–750 hPa) patterns of variables: (a) specific humidity, (b) moisture transport, (c) moisture source (evaporation – precipitation), and (d) total (horizontal plus vertical) moisture source. All the source terms are converted into specific humidity ( $\text{g kg}^{-1}$ ). (e) Daily fluctuation of 1000–750 hPa averaged specific humidity (SH), evaporation minus precipitation (SRC), and horizontal moisture transport (ADV) averaged over the region of sea ice reduction ( $21^\circ\text{--}79.5^\circ\text{E}$ ,  $75^\circ\text{--}79.5^\circ\text{N}$ ) in the Barents-Kara Seas (boxed area in Fig. 3.1a). The straight lines represent the winter means of individual variables..... 67
- Figure 4.16.** The winter-averaged lower-tropospheric (1000–900 hPa) patterns of (a) total heat, (b) heat transport, (c) turbulent (sensible + latent)

heat flux, and (d) greenhouse effect. All the terms are converted into temperature anomalies (K). (e) Daily fluctuation of 1000–900 hPa averaged temperature (AIR T), turbulent flux (FLX), radiation (RAD), and horizontal heat transport (ADV). The thick red curve is the sum of turbulent flux and radiation (SRC). The straight lines represent the winter means of individual variables. .... 68

**Figure 4.17.** The winter-averaged lower-tropospheric (1000–750 hPa) patterns of (a) total heat, (b) heat transport, (c) turbulent (sensible + latent) heat flux, and (d) greenhouse effect. All the terms are converted into temperature anomalies (K). (e) Daily fluctuation of 1000–750 hPa averaged temperature (AIR T), turbulent flux (FLX), radiation (RAD), and horizontal heat transport (ADV). The thick red curve is the sum of turbulent flux and radiation (SRC). The straight lines represent the winter means of individual variables. .... 69

**Figure 4.18.** (upper panel) The winter averaged lower tropospheric (1000–900 hPa) patterns of (a) total heating converted into temperature, and (b) atmospheric temperature. (lower panel) The same as the upper panel except for the pressure level of 1000–750 hPa. .... 70

**Figure 4.19.** Contributions of the horizontal and vertical processes to (a) moisture increase and (b) air temperature increase according to the level of budget closure in the lower troposphere. In (a; moisture budget case), horizontal moisture advection and moisture source (evaporation minus precipitation) are compared. In (b; heat budget case), horizontal heat advection and greenhouse effect induced by horizontal moisture advection is compared against the sum of turbulent heat flux and greenhouse effect induced by moisture source in the heat budget equation..... 71

# **Chapter 1. Introduction**

## **1.1. Background**

Over the past decades, rapidly enhanced atmospheric warming has been observed in the Arctic (Serreze and Francis, 2006; Bekryaev et al., 2010; IPCC, 2013). The accelerated warming is pronounced in the lower troposphere during the cold season (Serreze et al., 2009; Screen and Simmonds, 2010a; Screen et al., 2013). An accompanying drastic reduction of sea ice (Comiso et al., 2008; Comiso, 2012) has pronounced implications for global climate changes by affecting energy exchange between the ocean and the atmosphere (Serreze and Barry, 2011), and is often regarded as a key factor for accelerated warming in the Arctic (Holland and Bitz, 2003; Serreze et al., 2007; Screen and Simmonds, 2010a; Kumar et al., 2010). Physically, sea ice loss involves a positive ice-atmosphere feedback, which leads to an enhanced warming signal in the Arctic region. This feature is generally referred to as Arctic amplification (Screen and Simmonds, 2010a; Serreze and Barry, 2011) and is expected to persist at least for the next decade (IPCC, 2013; Koenigk et al., 2013).

A particularly significant sea ice reduction can be found over the Barents and Kara Seas, which potentially influences cold winter extremes over the Eurasian continent (Petoukhov and Semenov, 2010; Overland et al., 2011; Tang et al., 2013; Cohen et al., 2014; Mori et al., 2014; Kim et al., 2014; Kim and Son, 2016). The Barents-Kara Seas are the only region in the Arctic Ocean, where wintertime sea ice reduction is conspicuous; other areas of the Arctic Ocean do not exhibit significant loss of sea ice during the winter (Kim et al., 2016; Yang et

al., 2016). Sea ice cover has dwindled by  $\sim 50\%$  during the past 40 years and it seems to be continuing at a faster rate (Cavalieri and Parkinson, 2012; Serreze and Stroeve, 2015; Kim et al., 2016). At the same time, lower tropospheric winter temperature has risen by  $\sim 2\text{K}$  during the same time interval (Connolly et al., 2017; Johannessen et al., 2016; Kim et al., 2016).

Previous studies have proposed the physical mechanisms of Arctic amplification, which involve the effect of atmospheric heat transport (Graversen et al., 2008), oceanic heat transport (Årthun et al., 2012; Chylek et al., 2009; Spielhagen et al., 2011; Onarheim et al., 2015), cloud and water vapor changes (Francis and Hunter, 2007; Schweiger et al., 2008; Park et al., 2015a; Park et al., 2015b), and/or diminishing sea ice cover (Serreze et al., 2009; Screen and Simonds, 2010a; Kim et al., 2016). The accurate physical process of the Arctic amplification, however, is subject to debate.

Due to the large seasonal variation of insolation, there exists pronounced seasonality in the air-sea interaction process over the Arctic Ocean. During summer, open water readily absorbs solar radiation, which results in increased heat content in the oceanic mixed layer. This represents the so-called albedo feedback (Deser et al., 2000; Serreze et al., 2009; Screen and Simmonds., 2010a; Deser et al., 2010; Serreze and Barry, 2011), meaning that the Arctic Ocean is efficient in absorbing radiation energy during summer. The albedo feedback is also important during the snow and ice melt in spring and early summer even before the appearance of open sea. After the sun sets over the Arctic Ocean, the ice-albedo feedback is suppressed and the primary air-sea interaction mechanism becomes oceanic horizontal advection and vertical

convection of heat (Screen and Simmonds, 2010b). The stored heat in the ocean mixed layer is released back to the colder atmosphere above, which will result in warming of the atmosphere. The decreased insulation effect (Screen and Simmonds, 2010b) due to the loss of sea ice also promotes further sea ice reduction. Thus, heat transfer between the ocean and atmosphere is generally considered as the fundamental mechanism of Arctic amplification, which is pronounced only during the cold season. On the other hand, increased cloud cover and water vapor (Francis and Hunter, 2007; Schweiger et al., 2008; Graversen and Wang, 2009; Park et al., 2015a; Park et al., 2015b; Cao et al., 2017) can also contribute to an increase in downward longwave radiation.

Despite the general consensus that heat transfer between the ocean and atmosphere is a crucial element in the physical mechanism of Arctic amplification and sea ice reduction, a quantitative understanding of individual contributions of heat flux components is still controversial. Further, the role of upward and downward longwave radiation in Arctic amplification is vague and is not fully understood. Accurately quantifying the contribution of these different mechanisms, therefore, is required for a complete understanding of the Arctic amplification.

Previous studies showed that the temporal pattern of sea ice variation indeed differs significantly between the Barents–Kara Seas and the Laptev and Chukchi Seas (Kim et al., 2016; Yang et al., 2016). Sea ice reduction in the Barents-Kara Seas persists throughout the year, in contrast to the seasonality of sea ice variations in the other Arctic sea areas. Sea ice refreezes and the sea surface exposed to air is closed up in late fall in the Laptev and Chukchi seas. As

a result, significant absorption of solar radiation in summer does not lead to increased turbulent heat flux in winter. However, sea surface does not freeze up completely in the Barents–Kara Seas. Consequently, turbulent heat flux becomes available in winter in the Barents–Kara Seas for heating the atmospheric column, which in turn increases downward longwave radiation. Kim and Kim (2017) also showed that the major drivers for increases in downward longwave radiation and precipitable water differ regionally. In the northern Greenland Sea, increasing downward longwave radiation and moisture are caused mainly by convergence of atmospheric energy transport from lower latitudes. In regions of maximum sea ice retreat (e.g., Barents-Kara Seas), continued sea ice melting from previous seasons drives the downward longwave radiation increase, consistent with the positive ice-insulation feedback.

Most studies agree that increasing downward longwave radiation due to atmospheric warming is the essential factor for the continuing reduction of sea ice. Meanwhile, there are different explanations for the cause-and-effect relationship between the sea ice reduction and the lower tropospheric warming over the Barents-Kara Seas. Park et al. (2015a) suggested that the increase in downward longwave radiation is primarily due to horizontal advection of water vapor and heat energy into the Arctic from lower latitudes, rather than evaporation from the Arctic Ocean. Park et al. (2015b) suggested that northward flux of moisture into the Arctic is connected with enhanced convection over the tropical Indian and western Pacific Ocean, and that this northward flux of moisture increases downward longwave radiation.

Burt et al. (2016), on the other hand, showed that the simulated moistening of the Arctic atmosphere during winter is primarily due to an increase in surface evaporation rather than poleward moisture transport. Kurita (2011) analyzed the source region of Arctic water vapor during the ice-growth season and reported that local moisture source is dominant during late fall and early winter but moisture transport from lower latitudes becomes more important than local source after early winter. Therefore, relative role of vertical processes resulting from the reduction of sea ice in the Barents-Kara Seas to horizontal advective processes is not yet clearly understood.

## **1.2. Objectives**

As described above, wintertime sea ice reduction is conspicuous over the Barents and Kara Seas. However, several physical mechanisms are proposed to explain the wintertime sea ice reduction and the lower tropospheric warming over the Arctic region.

In the present study, energy flux involved in the Arctic amplification is quantitatively assessed in relation to the sea ice reduction over the Barents and Kara Seas. For this goal, cyclostationary empirical orthogonal function (CSEOF) analysis is carried out on surface and pressure-level variables derived from the ERA interim daily reanalysis data in winter (Dec. 1–Feb. 28,  $d = 90$  days).

In the first part of the thesis (chapter 3), detailed physical mechanism of Arctic amplification and sea ice reduction in winter is identified. The primary goal is to extract a physically meaningful warming/sea ice reduction signal in

the Arctic region and to investigate how sea ice loss and individual energy flux are linked in a quantitative manner.

In the second part of the thesis (chapter 4), relative role of vertical processes resulting from the reduction of sea ice in the Barents-Kara seas to horizontal advective processes is investigated. In particular, thermal energy and moisture budgets are analyzed over the region of sea ice reduction in order to delineate the relative roles of horizontal and vertical processes. Moisture budget equation is used to compare the horizontal moisture advection term and vertical source of evaporation minus precipitation in explaining specific humidity change in the atmospheric column. Thermal energy budget equation is used to assess the relative importance of horizontal heat advection and vertical source of energy from the release of turbulent heat fluxes and radiation trapped in the atmospheric column. Moreover, moist static energy budget is analyzed in the same way in order to consider heat and moisture changes simultaneously in the atmospheric column.



## Chapter 2. Data and Methodology

### 2.1. Data

ECMWF Reanalysis (ERA) interim daily variables are used from 1979–2018 (Dee et al. 2011). Both surface and pressure-level variables during winter (Dec. 1–Feb. 28; 90 days) are analyzed over the Arctic region (north of 60° N) to understand the detailed physical mechanism of wintertime sea ice loss and Arctic amplification. Winter (DJF) is chosen as the target period since it is the season of maximum sea ice reduction and Arctic warming over the Barents-Kara Seas (Kim et al., 2016).

### 2.2. Methodology

Analysis tool used for this study is the CSEOF technique (Kim et al., 1996; Kim and North, 1997; Kim et al., 2015; Kim, 2017). In CSEOF analysis individual physical processes in space-time data are decomposed as:

$$T(r, t) = \sum_n B_n(r, t) T_n(t), \quad B_n(r, t) = B_n(r, t + d), \quad (1)$$

where  $B_n(r, t)$  depicts daily winter evolution of the  $n$ th physical process and  $T_n(t)$  describes how the amplitude of the evolution varies on a longer time scale, and  $r$  and  $t$  denote location and time, respectively. Since the nested period is  $d = 90$  days, each loading vector,  $B_n(r, t)$ , consists of 90 spatial patterns which depict evolution of a variable throughout the winter. These winter evolution patterns,  $B_n(r, t)$ , repeat every winter, but its amplitude varies from one year to another according to the corresponding principal

component (PC) time series. CSEOF loading vectors are mutually orthogonal to each other in space and time and represent distinct physical processes. The PC time series,  $T_n(t)$ , are uncorrelated with (and are often nearly independent of) each other. Each loading vector depicts a temporal evolution of spatial patterns seen in a physical process (such as El Niño or seasonal cycle), and corresponding PC time series describes a long-term modulation of the amplitude of the physical process. Thus, the CSEOF technique is suitable for extracting and depicting temporal evolution of (nearly independent) physical processes and often yields valuable insight that cannot be attained from single spatial pattern.

In order to make suitable physical interpretation of the analysis results, CSEOF analysis is conducted on a number of key variables. It is, then, important to make CSEOF loading vectors derived from individual variables to be physically consistent with each other. For the purpose of generating physically consistent CSEOF loading vectors, regression analysis is carried out in CSEOF space (Kim et al., 2015). A target variable is chosen such that its major CSEOF mode best depicts the physical process under investigation; target variable is sea ice concentration in the present study.

Once CSEOF analysis on the “target” variable is completed as in equation (1), physically consistent loading vectors of another variable, called the “predictor” variable, are obtained as follows:

Step 1: CSEOF analysis on a new variable

$$P(r, t) = \sum_n C_n(r, t) P_n(t), \quad (2)$$

Step 2: regression analysis on a target PC time series

$$T_n(t) = \sum_{m=1}^M \alpha_m^{(n)} P_m(t) + \varepsilon^{(n)}(t), \quad (3)$$

Step 3: construction of regressed loading vector

$$C_n^{(reg)}(r, t) = \sum_{m=1}^M \alpha_m^{(n)} C_m(r, t). \quad (4)$$

Then, the target and predictor variables together can be written as

$$\{T(r, t), P(r, t)\} = \sum_n \{B_n(r, t), C_n^{(reg)}(r, t)\} T_n(t). \quad (5)$$

Namely, the loading vectors of the two variables,  $B_n(r, t)$  and  $C_n^{(reg)}(r, t)$ , share an identical PC time series,  $T_n(t)$ , for each mode  $n$ . As a result, the evolution of a physical process manifested as  $B_n(r, t)$  and  $C_n^{(reg)}(r, t)$  in two different variables is governed by a single amplitude time series. Otherwise,  $B_n(r, t)$  and  $C_n^{(reg)}(r, t)$  do not represent the same physical process and henceforth are not physically consistent. This process can be repeated for as many predictor variables as needed. As a result of regression, then, entire data can be written in the form

$$Data(r, t) = \sum_n \{B_n(r, t), C_n^{(reg)}(r, t), D_n^{(reg)}(r, t), \dots\} T_n(t), \quad (6)$$

where the terms in curly braces denote physically consistent evolutions derived from various physical variables. A rigorous mathematical explanation of the regression analysis in CSEOF space can be found in Kim (2017).

## **Chapter 3. Vertical feedback mechanism of winter Arctic amplification and sea ice loss**

### **3.1. CSEOF mode of Arctic amplification and sea ice loss**

Figures 3.1–3.4 show the sea ice loss mode identified through CSEOF analysis. Figure 3.1a is obtained based on a linear trend of sea ice concentration at each grid point based on the ERA-Interim sea ice concentration from 1979–2018 and Figure 3.1b shows the winter-averaged CSEOF loading pattern of sea ice concentration,  $B_1(r, t)$ . Since the loading vector (Fig. 3.1b) and the amplitude (PC) time series (Fig. 3.1c) describes sea ice reduction, together with natural variability of sea ice concentration, this mode represents the loss of sea ice in the Barents and Kara Seas during the past 39 years and explains ~25% of the total variability of the sea ice concentration in the Arctic Ocean. The pattern of sea ice reduction (Fig. 3.1b) is nearly identical with the trend pattern of sea ice concentration in the Arctic Ocean (Fig. 3.1a). As can be seen in Fig. 3.1d, the sea ice reduction trend in the Barents and Kara Seas (boxed area in Fig. 3.1a) is faithfully captured by this mode. In particular, the rate of sea ice loss has significantly increased since 2004-2005 (Vihma, 2014).

Figure 3.2 shows the patterns of decadal trend and the averaged regressed loading vector for the winter 2 m air temperature variations. The warming pattern of surface air derived from the regressed loading vector (Fig. 3.2b) is consistent with the trend in the 2 m air temperature (Fig. 3.2a). Therefore, conspicuous warming accompanies the sea ice reduction in the Barents-Kara Seas in the sea ice loss mode.

Figure 3.3 shows the winter-averaged pattern of  $B_1(r, t)$  together with the regressed patterns from other variables (the terms in the curly braces in (6)). In association with the sea ice loss, 2 m air temperature, 850 hPa temperature, specific humidity, upward longwave radiation, downward longwave radiation, and upward heat flux have increased significantly over the region of major sea ice reduction [ $21^\circ\text{--}79.5^\circ\text{E} \times 75^\circ\text{--}79.5^\circ\text{N}$ ] (boxed area in Fig. 3.2a). As can be seen in Figs. 3.3a, 3.3c and 3.3e, the central areas of anomalous 2 m air temperature, upward longwave radiation and turbulent (sensible + latent) heat flux match well with the region of sea ice loss in the Barents-Kara Seas (Screen and Simmonds, 2010b). On the other hand, the centers of the downward longwave radiation and lower-tropospheric specific humidity match well with that of the 850 hPa air temperature (Figs. 3.3b, 3.3d, and 3.3f).

Sea ice concentration varies slightly on a daily basis, and its fluctuation is less than 2% from the mean value of  $-14.7\%$  throughout the winter (Fig. 3.4). In accordance with the reduced sea ice concentration, upward longwave radiation flux is increased from the warmer sea surface exposed to air. Multiplying the amplitude time series (Fig. 3.1c) with the loading vector (Fig. 3.4) of the sea ice loss mode as in equation (1), actual sea ice concentration time series is obtained as in Fig. 3.1d. According to Fig. 3.1d, sea ice concentration has decreased by  $\sim 40\%$  during the last 39 years (1979-2018), and the rate of sea ice reduction appears to be accelerating. A curve fit with an exponential function results in

$$pc(t) = a\exp(\lambda t) + b = a(e^\lambda)^t + b \approx a(1 + \lambda)^t + b, \quad (7)$$

where  $pc(t)$  is the amplitude time series in Fig. 3.1c, and  $t$  is time in years since 1979. We obtained the fitting curve (dashed curve in Fig. 3.1d) with parameters  $a = 1.275 \times 10^{-1}$ ,  $\lambda = 8.916 \times 10^{-2}$ , and  $b = -9.055 \times 10^{-1}$ . Equation (7) can be rewritten as

$$pc(t) - c = (pc(0) - c)(1 + \lambda)^t. \quad (8)$$

That is, the amplitude of sea ice reduction and atmospheric warming increases at the rate of  $\sim 8.9$  % every year. Arctic warming tends to increase at this rate until sea ice concentration reaches a critical level of 10–20%. The rates of Arctic warming, however, may not necessarily accelerate once sea ice concentration reaches a critical level (Yim et al., 2016; Kim and Kim, 2017).

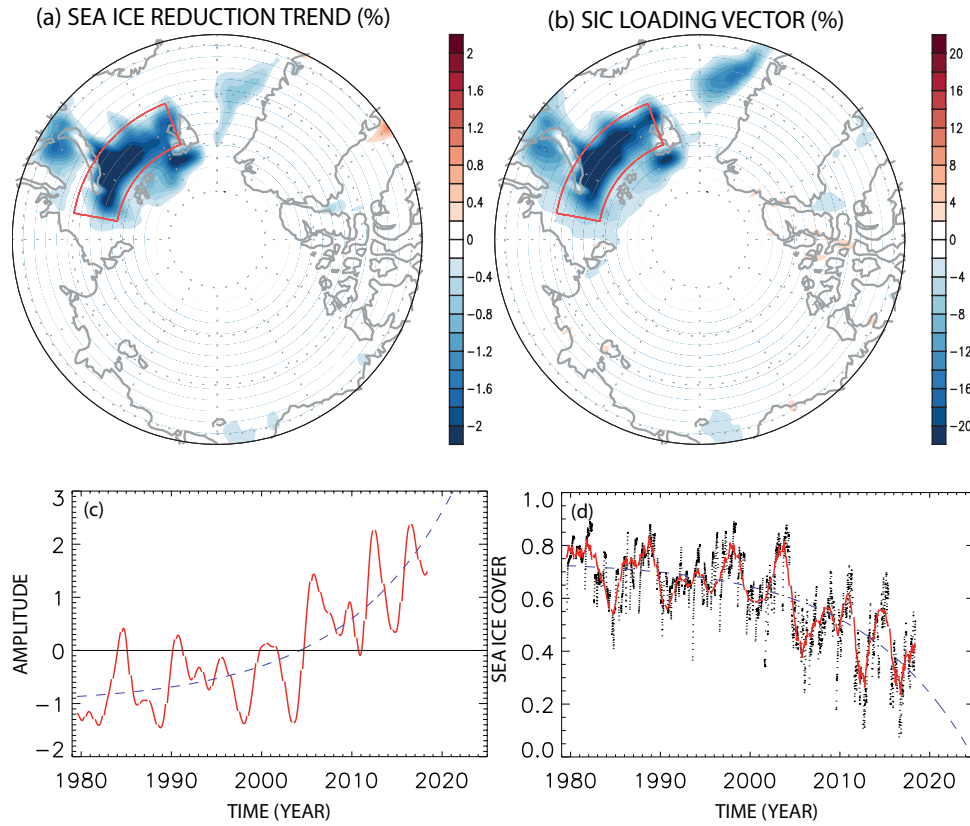


**Figure 3.1.** (a) The yearly trend (%) of winter sea ice reduction in the Arctic Ocean during 1979–2018, (b) the winter (Dec. 1–Feb. 28) averaged loading vector of the sea ice loss mode, (c) the corresponding PC (amplitude) time series (*red solid curve*) and amplification curve (*blue dashed curve*), and (d) actual sea ice concentration in the sea-ice loss region ( $21^{\circ}$ – $79.5^{\circ}$  E  $\times$   $75^{\circ}$ – $79.5^{\circ}$  N; the boxed area in (a) and (b)) of the Barents and Kara Seas (*black dotted curve*), sea ice concentration according to the sea ice loss mode (*red curve*) and a projection (*blue dashed curve*) based on the exponential fit of the amplitude time series in (c).

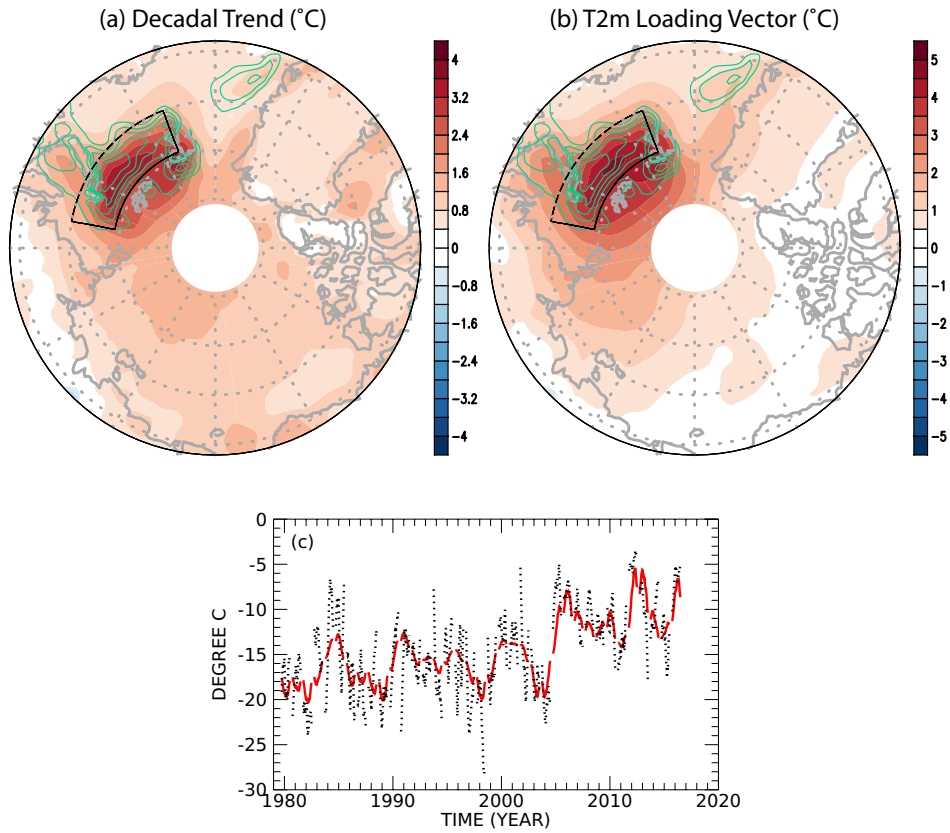


**Figure 3.2.** (a) The decadal trend (°C) of winter 2 m air temperature increase in the Arctic Ocean during 1979–2016, (b) the winter averaged loading vector of regressed 2 m air temperature in the sea ice loss mode, (c) 30 days moving averaged winter 2 m air temperature variations in the sea-ice loss region ( $21^{\circ}$ – $79.5^{\circ}$  E  $\times$   $75^{\circ}$ – $79.5^{\circ}$  N; the boxed area in (a) and (b)) of the Barents and Kara Seas; actual variation from the raw data (*black dotted curve*), reconstructed variation according to the sea ice loss mode (*red curve*). The green contours in (a)–(b) represent sea ice reduction in Fig. 3.1(b) (the same hereinafter).



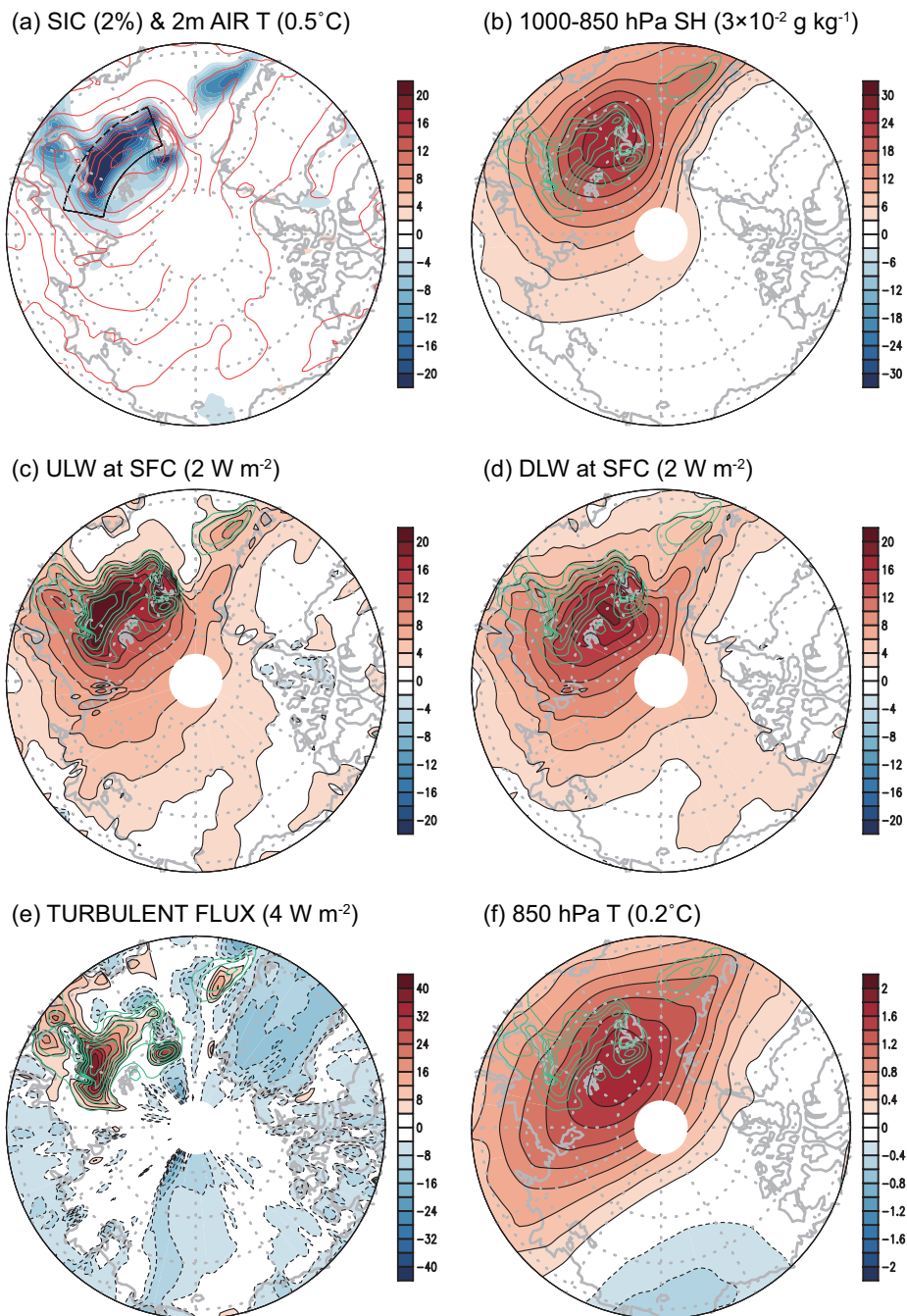


**Figure 3.3.** Winter averaged patterns of sea ice loss mode: (a) sea ice (*shading*) and 2 m air temperature (*contour*), (b) 1000–850 hPa specific humidity, (c) upward longwave radiation, (d) downward longwave radiation, (e) turbulent (sensible + latent) heat flux, (f) 850 hPa air temperature. The numbers in parenthesis are contour intervals and negative contours are dashed.

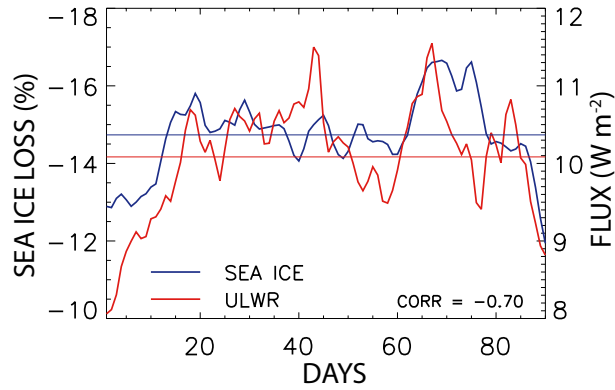


**Figure 3.4.** Anomalous daily sea ice concentration (*blue curve*) and upward longwave radiation (*red curve*) averaged over the region of sea ice loss ( $21^{\circ}$ – $79.5^{\circ}$  E  $\times$   $75^{\circ}$ – $79.5^{\circ}$  N) with respective mean values (*straight lines*). Winter days are counted from December 1.

Figure 3.5 shows the anomalous surface (2 m) air temperature, the lower tropospheric geopotential height and wind and the vertical cross section of anomalous temperature, geopotential height, wind and pressure layer thickness along 60°E and 80°N associated with the sea ice reduction. A significant warming is seen in the lower troposphere (e.g., Serreze and Francis, 2006; Serreze et al., 2007; Screen et al., 2013). The anomalous wind and geopotential height are consistent according to the thermal wind equation. The anomalous temperature and geopotential height are consistent according to the hydrostatic equation. The shaded geopotential height anomaly in Figs. 3.5e and 3.5f is obtained directly from the geopotential height field in Figs. 3.5c and 3.5d, i.e.,

$$(dZ)_j = Z_j - Z_{j-1}, \quad (9)$$

where  $j$  is an index for the vertical level. The contoured geopotential height anomaly in Figs. 3.4e and 3.4f is obtained from the temperature field in Fig. 3.4c and 3.4d, i.e.,

$$(dZ)_j = -\frac{R\langle T \rangle_j}{g}(d\ln p)_j, \quad (10)$$

where

$$\langle T \rangle_j = (T_j + T_{j-1})/2, \quad (d\ln p)_j = \ln p_j - \ln p_{j-1}. \quad (11)$$

As can be seen in Fig. 3.5, the anomalous geopotential height field is nearly in hydrostatic balance with the anomalous temperature field. The difference is partially due the use of layer mean temperature  $\langle T \rangle$  in a finite-difference approximation of the hydrostatic equation in (10). Thus, it seems that the release of energy in the form of radiation and heat flux changes the temperature,

and geopotential height in the lower troposphere adjusts in accordance with the hydrostatic balance. As can be seen, an anticyclonic circulation is established over the region of sea ice loss. This anticyclonic circulation results in advection of warmer air over the Barents and Kara Seas and advection of colder air over the mid-latitude East Asia (Kim and Son, 2016).

The winter-averaged patterns of anomalous downward longwave radiation and specific humidity look fairly similar to that of 850 hPa air temperature (Fig. 3.6 and Fig. 3.3). It appears that the increased downward longwave radiation is the result of the tropospheric warming (Fig. 3.5). Specific humidity also increases with the tropospheric warming. Note specifically that these changes are observed over or close to the region of sea ice reduction. The pattern of total cloud cover, however, differs significantly from that of sea ice reduction. Since cloud is a difficult variable to simulate accurately, we also examine total column liquid water and total column ice water, which are the key variables for the formation of clouds. The patterns of total column liquid water and total column ice water exhibit a strong response over the region of sea ice reduction although their centers of action are shifted toward the Greenland Sea (Fig. 3.6d). Therefore, we postulate that the increased downward longwave radiation is due to the increased 850 hPa air temperature and the greenhouse effect produced by the increased specific humidity and cloudiness to a lesser extent. Further note that net (upward minus downward) longwave radiation is positive over the region of major sea ice reduction, whereas it is slightly negative over the surrounding areas (Fig. 3.6c). Thus, at the surface level, there is a net loss of longwave energy over the region of sea ice reduction, while there is a net gain of longwave radiation over the surrounding area.

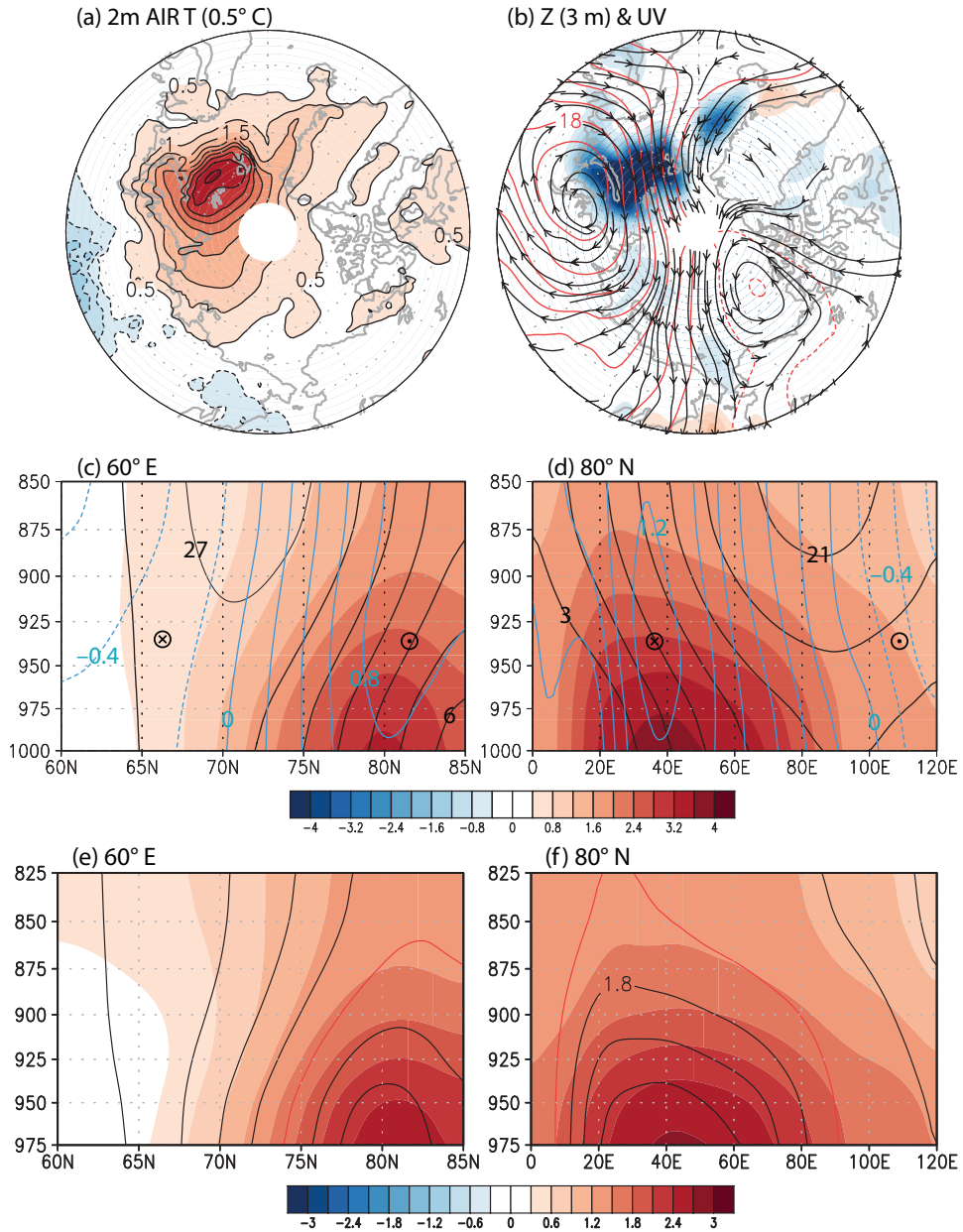


**Figure 3.5.** Winter-averaged patterns of anomalous atmospheric condition: (a) 2 m air temperature, contour interval is in parenthesis, (b) lower tropospheric (1000–900 hPa) geopotential height (*red contour*) and wind (*black arrow line*), sea ice reduction (% *shading*), (c) vertical cross section along 60° E of lower tropospheric (1000–850 hPa) air temperature, geopotential height and wind, and (d) along 80° N. Temperature is in shading (0.4 K), geopotential height is in black contours (3 m), and (c) zonal and (d) meridional winds are in blue contours (0.2 m s<sup>-1</sup>). (e and f) pressure layer thickness ( $\Delta Z = Z(p_1) - Z(p_0)$ ) derived from the geopotential height pattern in (c) and (d) (*shading*) and that

derived from the hydrostatic equation (*contour*). The red contour represents the thickness of 1.5 m. The level  $p_1$  is the level used for plotting and  $p_0$  is the pressure level below  $p_1$  at the interval of 25 hPa.

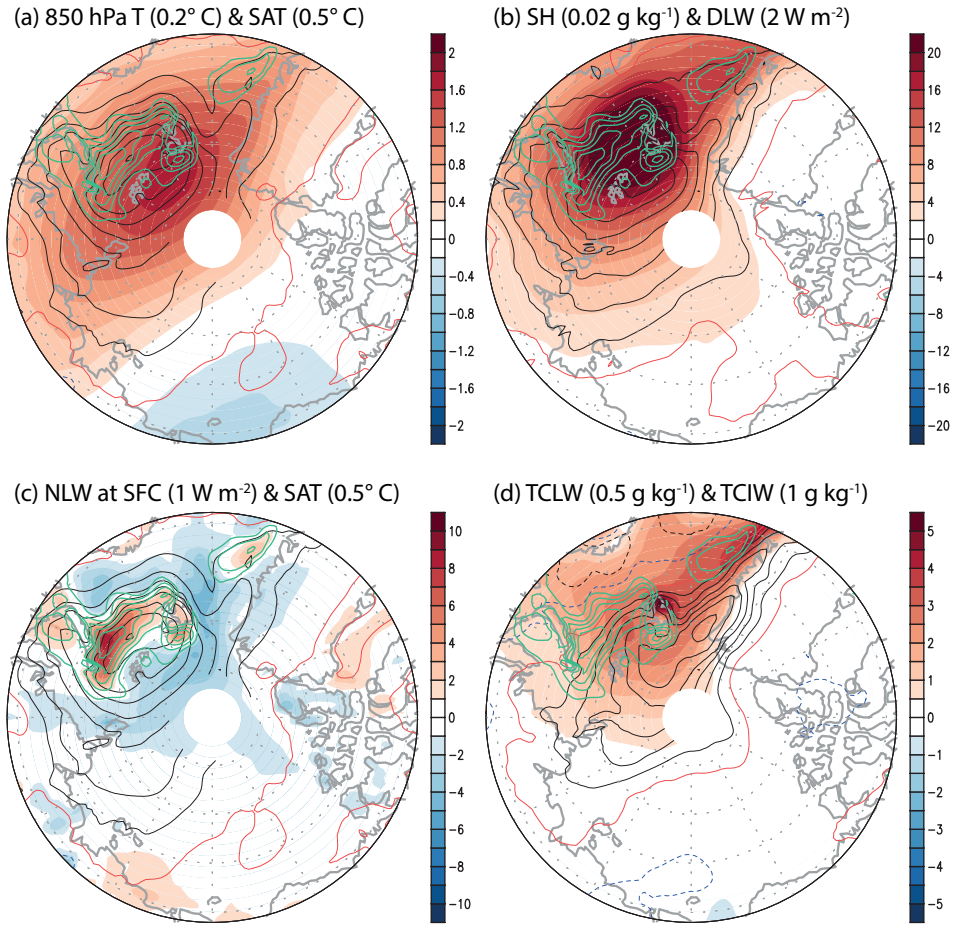


**Figure 3.6.** Winter-averaged patterns of (a) 850 hPa air temperature (*shading*) and 2 m air temperature (*contour*), (b) 900 hPa specific humidity (*shade*) and downward longwave radiation at surface (*contour*), (c) net (upward minus downward) longwave radiation at surface (*shade*) and SAT (*contour*), and (d) total cloud liquid water (*shading*) and total cloud ice water (*contour*) for the sea ice loss mode. The red contour is drawn at the value of the contour interval.

### 3.2. Sensitivity test on the choice of datasets

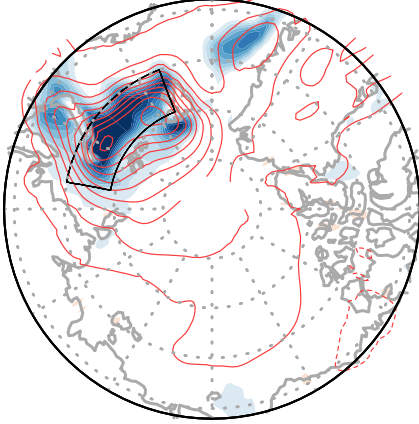
In this study, ERA-Interim reanalysis product is used to analyze sea ice concentration and several atmospheric variables in the Arctic region since it is difficult to obtain a comprehensive observational dataset. Reanalysis products, however, are notably inaccurate in the polar regions. Thus, the results discussed in the previous section have been reproduced using other reanalysis products in order to confirm that conclusions drawn in the present study are robust. Figures 3.7, 3.8 and 3.9 show the regressed loading vectors derived from the 1979-2016 NCEP reanalysis product, the 1979-2015 MERRA reanalysis products and 1979-2017 JRA-55 reanalysis product with the sea ice loss mode as the target. As a comparison among Figs. 3.7–3.9 and 3.3 (ERA-Interim) shows, there is no substantial difference between the three sets of regressed loading vectors except for a small difference in the scales. Figure 3.10 further shows the winter-averaged regressed loading vectors of precipitation and evaporation derived from the MERRA reanalysis product in comparison with those of the ERA-Interim reanalysis product with the respective sea ice loss mode as the target. It is shown that the loading patterns of precipitation and evaporation, difficult variables to simulate in reanalysis models, are rather similar between the two reanalysis products except for small differences in scales. This magnitude difference may be due to different sensitivity of sea ice to atmospheric and oceanic forcing in the two datasets.

This test confirms that the response characteristics of the atmospheric variables in association with the sea ice reduction in the Barents-Kara Seas are not significantly different among the reanalysis products and that the physical

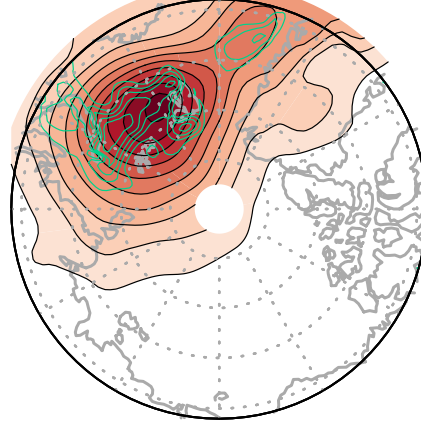


mechanism addressed in the present study is not overly sensitive to the choice of a reanalysis dataset. However, uncertainty is inherent in the quantitative estimates because of the use of a reanalysis product.

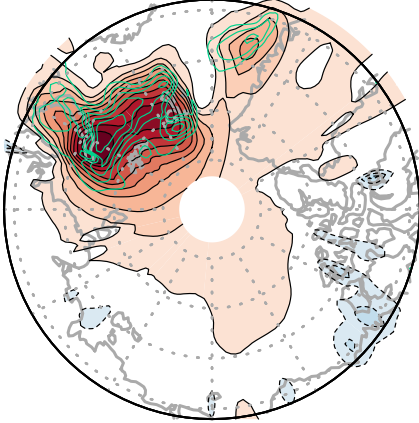
(a) SIC (2%) & 2m AIR T (0.5°C)



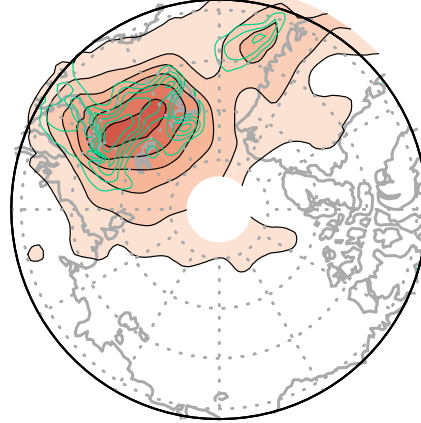
(b) 1000-850 hPa SH ( $3 \times 10^{-2} \text{ g kg}^{-1}$ )



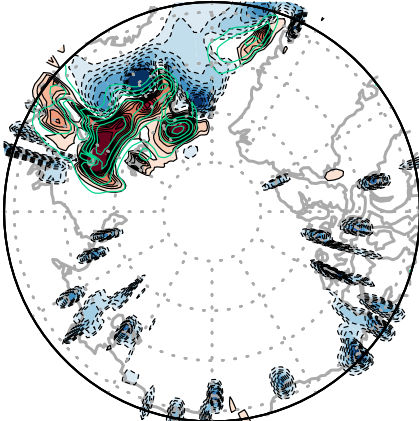
(c) ULW at SFC ( $2 \text{ W m}^{-2}$ )



(d) DLW at SFC ( $2 \text{ W m}^{-2}$ )



(e) TURBULENT FLUX ( $4 \text{ W m}^{-2}$ )



(f) 850 hPa T ( $0.2^\circ\text{C}$ )

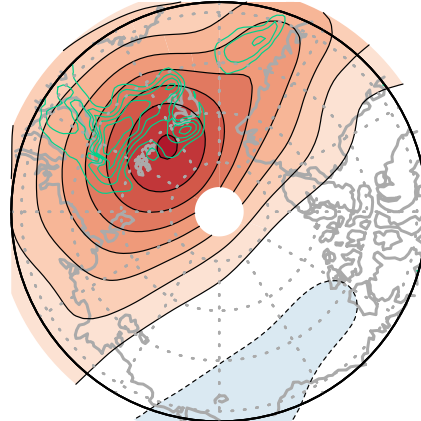
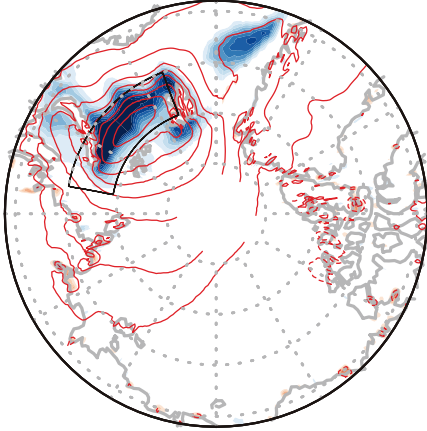
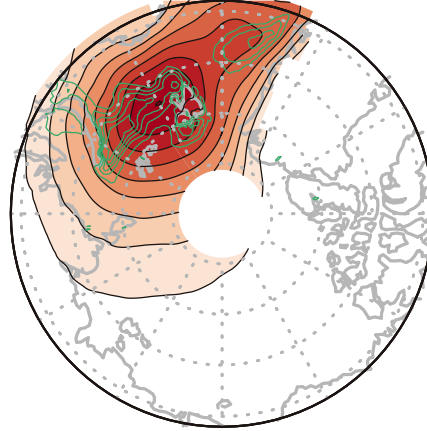


**Figure 3.7.** The regressed patterns of atmospheric variables based on the NCEP reanalysis product (1979-2016). The target is the sea ice loss mode.

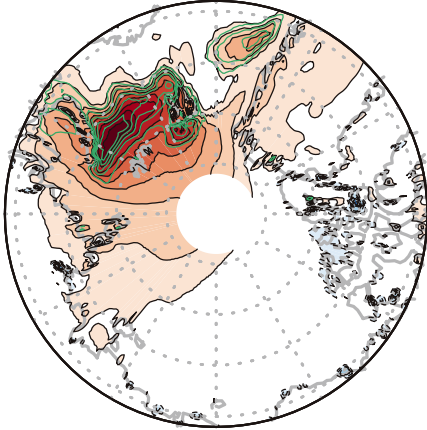
(a) SIC (2%) & 2m AIR T ( $0.5^{\circ}\text{C}$ )



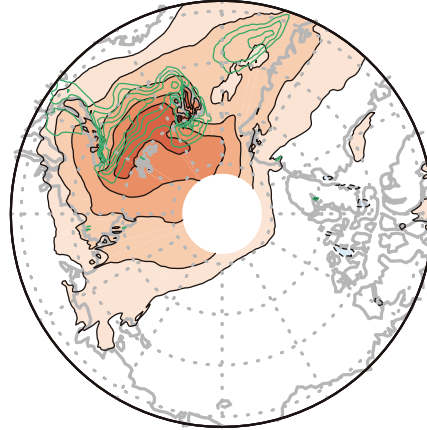
(b) 1000-850 hPa SH ( $3 \times 10^{-2} \text{ g kg}^{-1}$ )



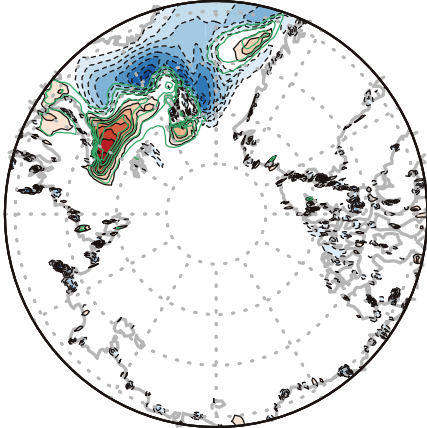
(c) ULW at SFC ( $2 \text{ W m}^{-2}$ )



(d) DLW at SFC ( $2 \text{ W m}^{-2}$ )



(e) TURBULENT FLUX ( $4 \text{ W m}^{-2}$ )



(f) 850 hPa T ( $0.2^{\circ}\text{C}$ )

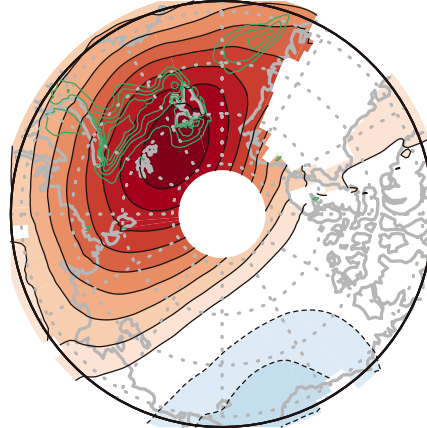
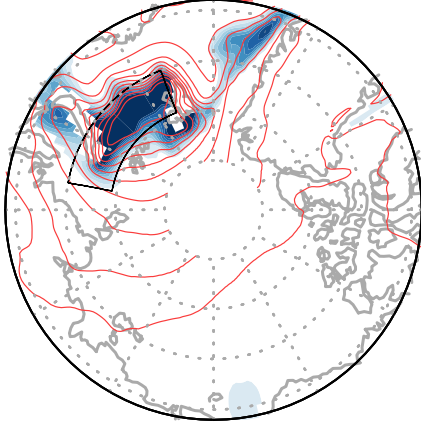
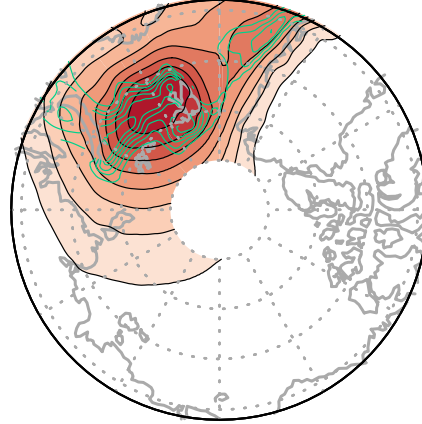


**Figure 3.8.** The regressed patterns of atmospheric variables based on the MERRA reanalysis product (1979-2015). The target is the sea ice loss mode.

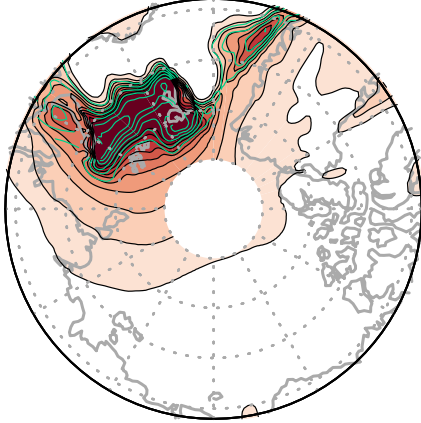
(a) SIC (2%) & 2m AIR T (0.5°C)



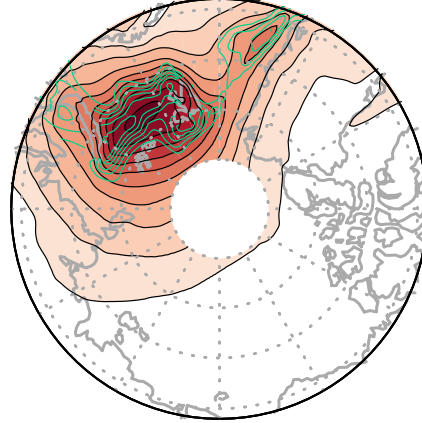
(b) 1000-850 hPa SH ( $3 \times 10^{-2} \text{ g kg}^{-1}$ )



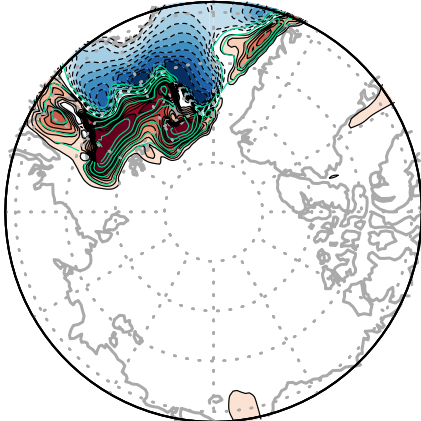
(c) ULW at SFC ( $2 \text{ W m}^{-2}$ )



(d) DLW at SFC ( $2 \text{ W m}^{-2}$ )



(e) TURBULENT FLUX ( $4 \text{ W m}^{-2}$ )



(f) 850 hPa T ( $0.2^\circ\text{C}$ )

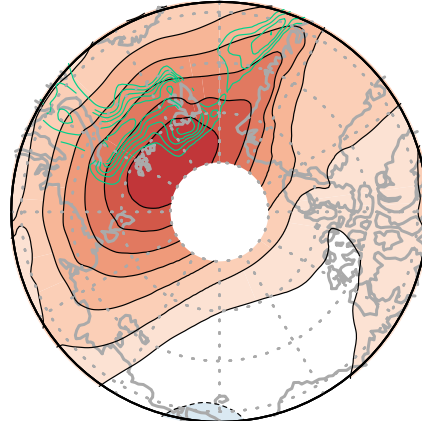


**Figure 3.9.** The regressed patterns of atmospheric variables based on the JRA-55 reanalysis product (1979-2017). The target is the sea ice loss mode.

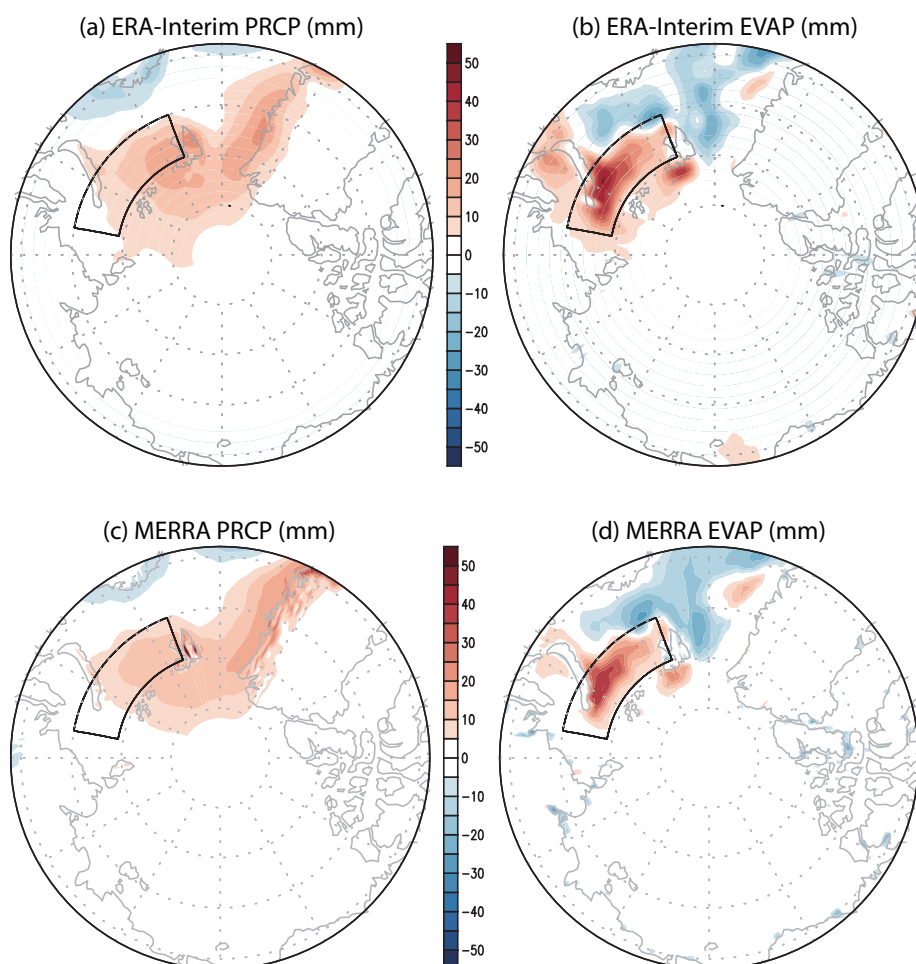


**Figure 3.10.** The winter (DJF) (a) total precipitation (mm) and (b) evaporation (mm) for the sea ice loss mode based on the ERA-Interim reanalysis product, (c) total precipitation (mm) and (d) evaporation (mm) based on the MERRA reanalysis product (1979-2015).

### 3.3. Vertical feedback mechanism

A prominent source of energy available for heating the atmospheric column is the increased turbulent heat flux from the sea surface exposed to air due to sea ice reduction (Fig. 3.11). Figure 3.12 shows the winter daily variations of the regressed loading vectors in (6) (terms in curly braces) averaged over the region of sea ice reduction ( $21^{\circ}$ – $79.5^{\circ}$  E  $\times$   $75^{\circ}$ – $79.5^{\circ}$  N); it may be interpreted as the atmospheric response to the sea ice reduction shown in Fig. 3.4. Although the total (area-weighted) magnitudes of sensible and latent heat fluxes are generally smaller than those of upward and downward longwave radiation (see Fig. 3.12a), turbulent heat flux (see Fig. 3.11) is locally more pronounced than longwave radiation (Deser et al., 2010). Furthermore, the combined effect of turbulent heat flux is about 6 times larger than that of longwave radiation, since upward and downward longwave radiation tends to offset each other and the resulting net longwave radiation is comparatively smaller than the net upward turbulent heat flux (Fig. 3.12a). In the presence of turbulent heat flux, air temperature and, henceforth, downward longwave radiation can increase continually leading to further sea ice reduction.

While the increased downward longwave radiation is a key element of sea ice reduction, it is not a sustainable physical process by itself. The area-averaged magnitudes of the upward and downward longwave radiation exceed those of the sensible and latent heat flux in the Barents and Kara Seas (Fig. 3.12a). The net amount of upward longwave radiation, however, is much smaller than the net upward heat flux as a result of near cancellation between the upward and downward longwave radiation. In fact, the upward radiation is, in

general, slightly larger than the downward radiation resulting in the net upward longwave radiation of  $\sim 2 \text{ W m}^{-2}$  in winter in the Barents and Kara Seas. This implies that surface temperature should decrease. A decrease in surface air temperature also means that upward longwave radiation decreases and, as a result, tropospheric air temperature decreases as well. In this sense, longwave radiation alone is not sufficient to sustain the sea ice reduction process. On the other hand, the net amount of heat flux is  $\sim 12 \text{ W m}^{-2}$  in the same area. Once ocean surface is exposed due to the reduction of sea ice by ocean current (Schlichtholz, 2011; Smedsrud et al., 2013) or wind (Park et al., 2015b), the enhanced turbulent heat flux helps sustain sea ice reduction by increasing downward longwave radiation. However, the release of turbulent heat flux can continue only when sea surface remains to be free of ice. While an accurate energy budget is difficult to evaluate in the context of data analysis, Fig. 3.1 indicates that open sea surface area tends to increase in time, leading to increasing turbulent heat flux from the surface in the Barents-Kara Seas. This indicates that sea ice is not fully recovered every year and turbulent heat flux increases as open sea surface area expands. Heat transport by the warm Norwegian current may be a likely mechanism for keeping sea surface from freezing (Årthun et al., 2012; Onarheim et al., 2015; Schlichtholz, 2011; Smedsrud et al., 2013).

As can be seen in Figs. 3.12b and 3.12c, daily upward longwave radiation change over the sea ice loss region is highly correlated with the daily fluctuation of 2 m air temperature, whereas daily downward longwave radiation change is strongly correlated with both 850 hPa and 2 m air temperatures. Moreover,

these variables have the spectral peaks near frequency of 4 and 16 days (Fig. 3.13). According to the lagged correlations (Fig. 3.14), daily changes of both upward and downward longwave radiation in the sea ice loss mode are highly correlated with those of 2 m air temperature and 850 hPa air temperature to a lesser extent. Based on the 3-hourly ERA-Interim data, 850 hPa air temperature turns out to lead changes in downward longwave radiation. Change in 2 m air temperature, on the other hand, is nearly simultaneous with the downward longwave radiation, whereas it slightly leads the upward longwave radiation. It appears that the increased tropospheric temperature increases the downward longwave radiation, which leads to further sea ice reduction. As a result, surface temperature and upward longwave radiation may increase.



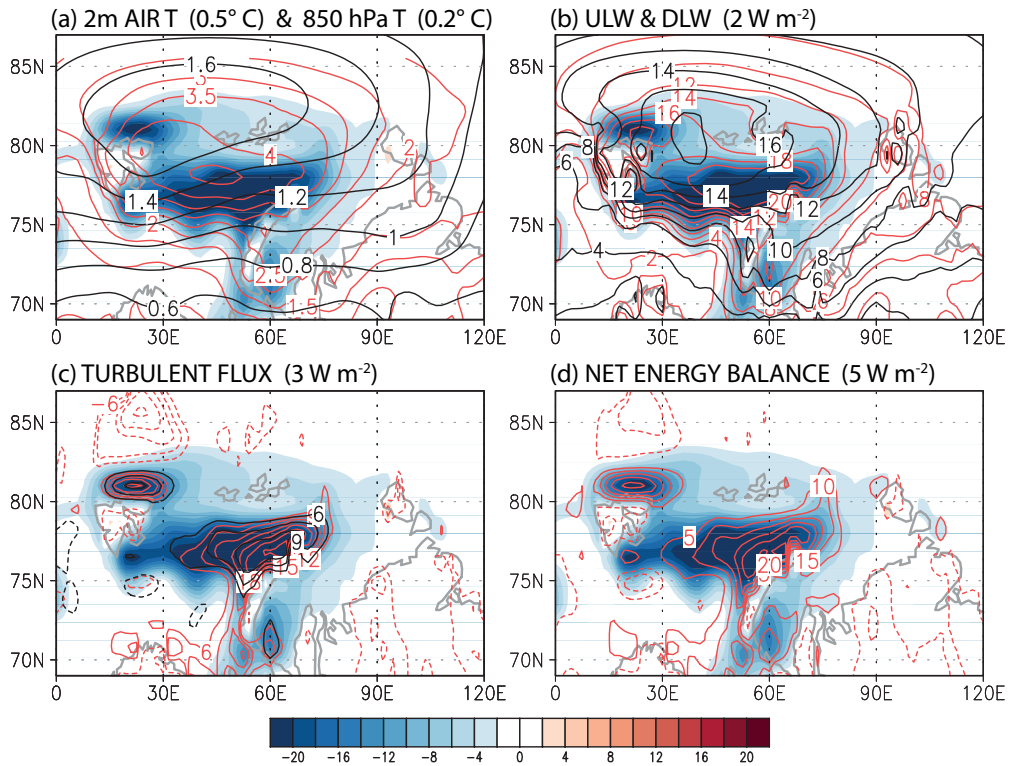


**Figure 3.11.** Winter average pattern of sea ice loss mode in the Barents and Kara Seas: (a) sea ice reduction (%), *shading*), 2 m air temperature (*red contour*) and 850 hPa temperature (*black contour*), (b) upward longwave radiation (*red contour*) and downward longwave radiation (*black contour*), (c) sensible heat flux (*red contour*) and latent heat flux (*black contour*), and (d) net energy balance (sensible heat flux + latent heat flux + upward longwave radiation – downward longwave radiation).

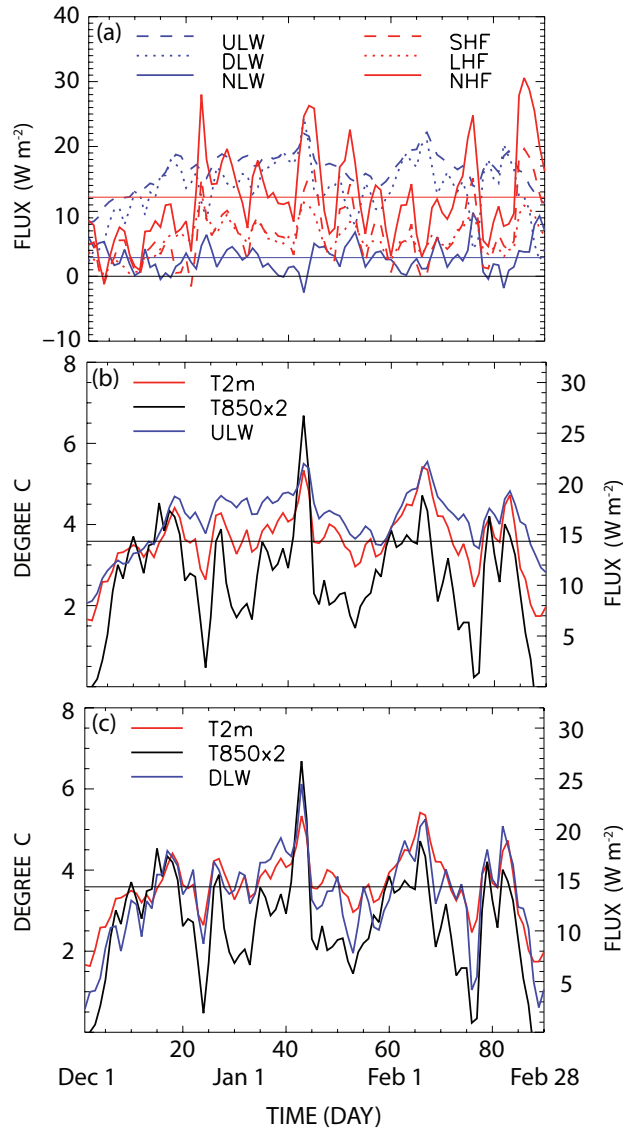


**Figure 3.12.** Daily patterns of variability over the region of sea ice loss ( $21^{\circ}$ – $79.5^{\circ}$  E  $\times$   $75^{\circ}$ – $79.5^{\circ}$  N): (a) upward longwave radiation (*blue dashed*), downward longwave radiation (*blue dotted*), net longwave radiation (*blue solid*) with its mean value (*blue straight line*), sensible heat flux (*red dashed*), latent heat flux (*red dotted*), and turbulent heat flux (*red solid*) with its mean value (*red straight line*), (b) 2 m air temperature (*red*), 850 hPa air temperature  $\times$  2 (*black*), and upward longwave radiation (*blue*), and (c) same as (b) except for the regressed downward longwave radiation (*blue*). The straight lines in (b) and (c) represent the winter mean value of anomalous 2 m air temperature. Correlation of upward and downward longwave radiation with 2 m air temperature is respectively 0.88 and 0.91, whereas with 850 hPa air temperature is 0.66 and 0.85.

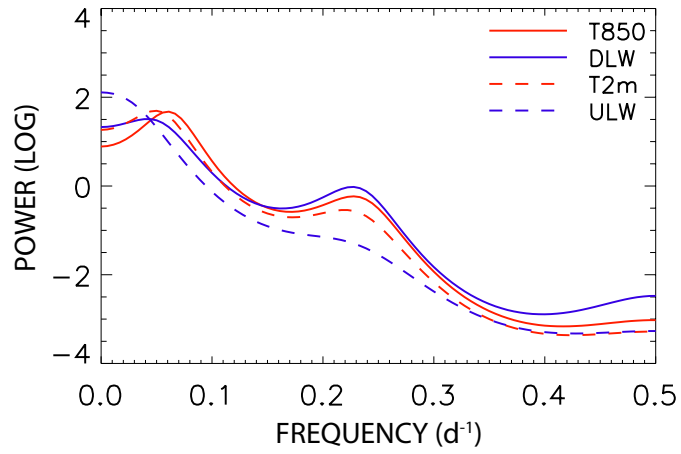


**Figure 3.13.** Periodogram of upward longwave radiation (*blue dashed*), downward longwave radiation (*blue*), 2 m air temperature (*red dashed*) and 850 hPa air temperature (*red*).

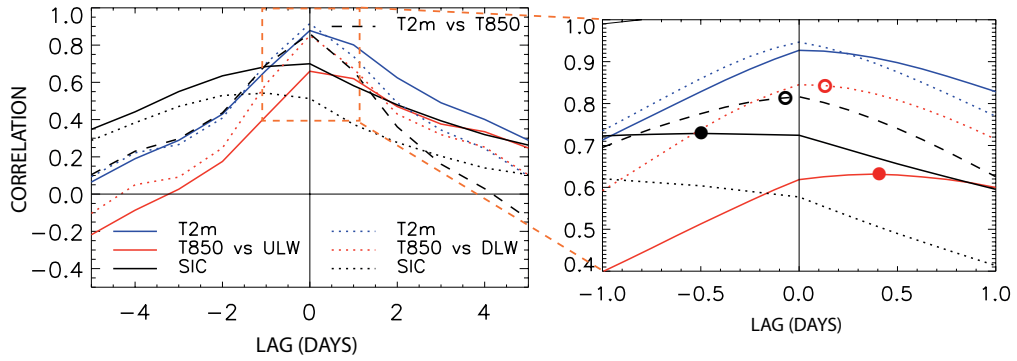


**Figure 3.14.** Lagged correlations: (a) correlation of upward (*solid lines*) and downward (*dotted lines*) longwave radiations with 2 m air temperature (*blue*), 850 hPa temperature (*red*), and sea ice concentration (*black*), and (b) a blowup of the boxed region in (a). Longwave radiation lags the other variable for a positive lag. Lagged correlation between 2 m air temperature and 850 hPa air temperature (*black dashed line*); 2 m air temperature leads 850 hPa temperature for a positive lag.

Therefore, the feedback mechanism is proposed as suggested in Fig. 3.15. Sea ice reduction in this area leads to an increase in upward heat flux, which is used to raise temperature in the lower troposphere. Warming in the lower troposphere increases downward longwave radiation. As a result, sea ice reduction is accelerated. This feedback process can be written mathematically as follow:

$$\begin{aligned} \text{Step 1: } \frac{dFL^{\uparrow(n)}}{dt} &= -\alpha \frac{ds^{(n)}}{dt}, \\ \text{where } FL^{\uparrow} &= SW^{\uparrow} - SW^{\downarrow} + LW^{\uparrow} - LW^{\downarrow} + SF^{\uparrow} + LF^{\uparrow}, \end{aligned} \quad (12)$$

$$\text{Step 2: } \frac{dT^{(n)}}{dt} = \beta \frac{dFL^{\uparrow(n)}}{dt}, \quad (13)$$

$$\text{Step 3: } \frac{dLW^{\downarrow(n)}}{dt} = \gamma \frac{dT^{(n)}}{dt}, \quad (14)$$

$$\text{Step 4: } \frac{ds^{(n+1)}}{dt} = -\delta \frac{dLW^{\downarrow(n)}}{dt}, \quad (15)$$

where  $S$  is sea ice concentration,  $T$  is tropospheric (850 hPa) temperature,  $LW^{\downarrow}$  is downward longwave radiation, and the net upward flux  $FL^{\uparrow}$  is the sum of net short and longwave radiation and sensible and latent heat fluxes. It is emphasized that sea ice reduction continues, since downward longwave radiation continues to increase via enhanced upward heat flux from the exposed sea surface. According to the proposed model, 1 % reduction in sea ice coverage leads to  $1.02 \text{ W m}^{-2}$  increase in upward energy flux, which, in turn, leads to  $0.09 \text{ K}$  increase in 850 hPa air temperature and  $0.91 \text{ W m}^{-2}$  increase in downward longwave radiation. This process is being amplified according to the PC time series in Fig. 3.1c. As sea ice concentration dwindles as in Fig. 3.1d, turbulent

heat flux and upward longwave radiation increase and, as a result, the lower tropospheric temperature and downward longwave radiation increase.

This proposed feedback mechanism, in its present form, does not require any delayed action of increased absorption of insolation during summer in terms of albedo feedback. In winter, a significant amount of turbulent heat flux can be released from the ocean exposed to cold air without excessive energy stored in summer. Summer heating, on the other hand, may be a fortifying factor for this feedback loop by preventing sea ice from refreezing during fall and winter.

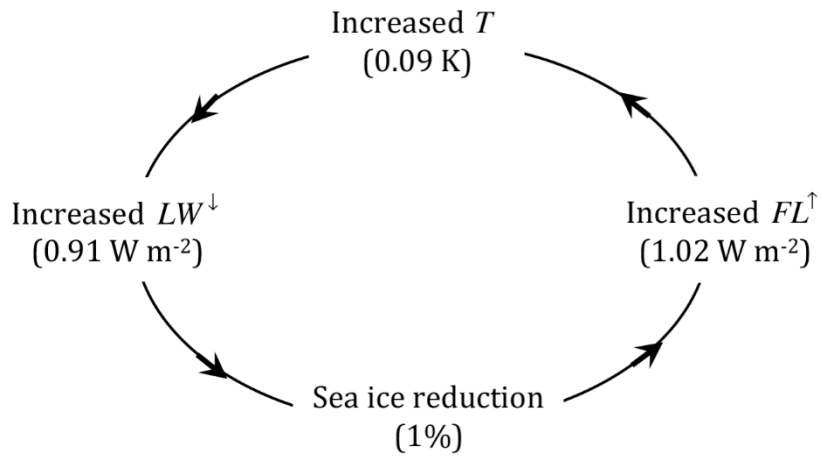


**Figure 3.15.** A proposed feedback mechanism of Arctic amplification. Increased net upward energy flux increases air temperature. As a result, downward longwave radiation increases, which results in sea ice reduction. This loop seems to amplify by  $\sim 8.9\%$  annually.

## **Chapter 4. Relative roles of horizontal and vertical processes in the physical mechanism of winter**

### **Arctic amplification**

The atmospheric warming is strongly confined to the lower troposphere over the region of sea ice reduction (Figs. 3.4 and 4.1) and the increased specific humidity is also evident (Fig. 4.1b). Calculation based on the Clausius-Clapeyron relationship (Iribarne and Godson, 1981; North and Erukhimova 2009) shows that the increased saturation specific humidity owing to the increased air temperature is commensurate in magnitude with the increased specific humidity. Figure 4.1 shows that the winter-averaged patterns of specific humidity are similar to those of air temperature and saturation specific humidity. Note that significant increase in temperature and specific humidity is confined to lower troposphere. As a result of sea ice reduction, turbulent heat flux is increased. Due to an increased exposition of warmer sea surface, upward longwave radiation increases, whereas downward longwave radiation also increases due to increased lower tropospheric temperature. In the previous chapter, contribution of this vertical feedback mechanism to sea ice loss has been estimated.

Figure 4.2 shows the regressed pattern of moisture and heat advection. As can be seen, there are net convergence of moisture transport and heat transport over the region of sea ice reduction, although the center of action is over the Greenland Sea. Thus, moisture and heat transport from lower latitudes apparently affects the variation of sea ice concentration, and it seems that both



the convergence of moisture transport and the convergence of heat transport are at least partly responsible for the variation of specific humidity and temperature in the lower troposphere. Therefore, it is necessary to compare the relative importance of the vertical process and the horizontal advection. In this chapter, moisture and heat budget analysis is carried out to compare the horizontal advective process against the vertical feedback process.

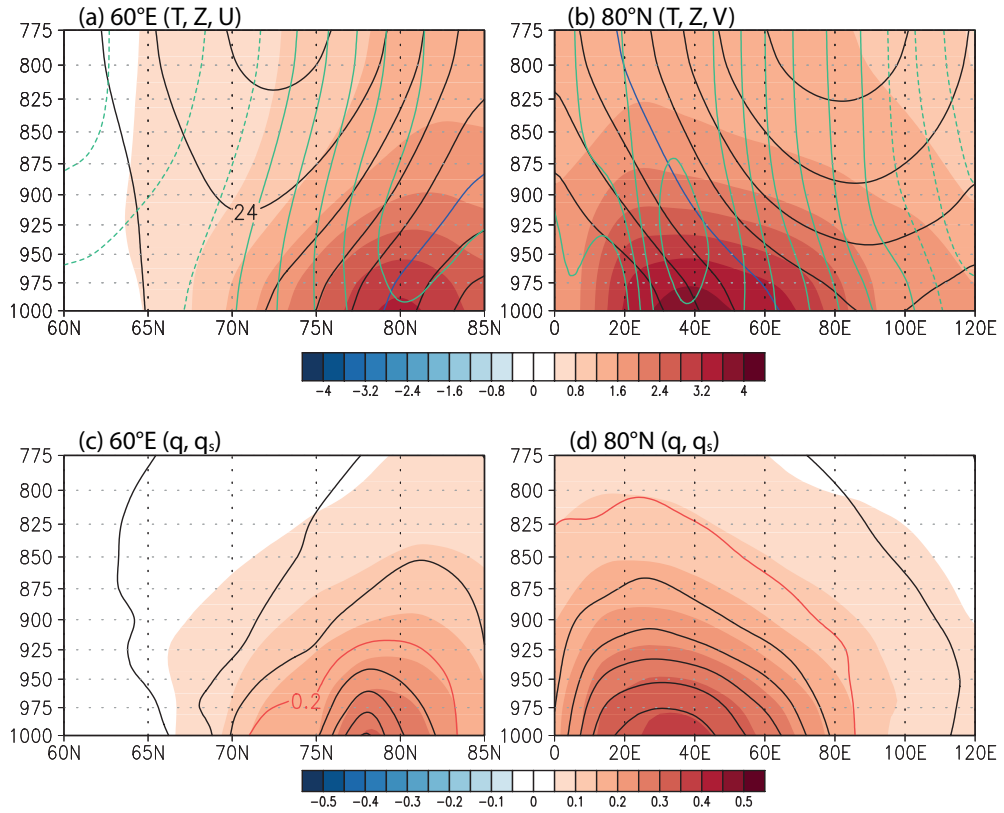


**Figure 4.1.** (a and b) The vertical pattern of winter-averaged (temperature (*shading*), geopotential (*black contour*; 3 m<sup>2</sup> s<sup>2</sup>) and wind (*green contour*; 0.2 m s<sup>-1</sup>), and (c and d) specific humidity (*shading*) and saturation specific humidity (*contour*; 0.05 g kg<sup>-1</sup>) along 60°E and 80°N. The blue contour in the upper panel is at 12 m<sup>2</sup> s<sup>2</sup>. The red contour in the lower panel is at 0.2 g kg<sup>-1</sup>.

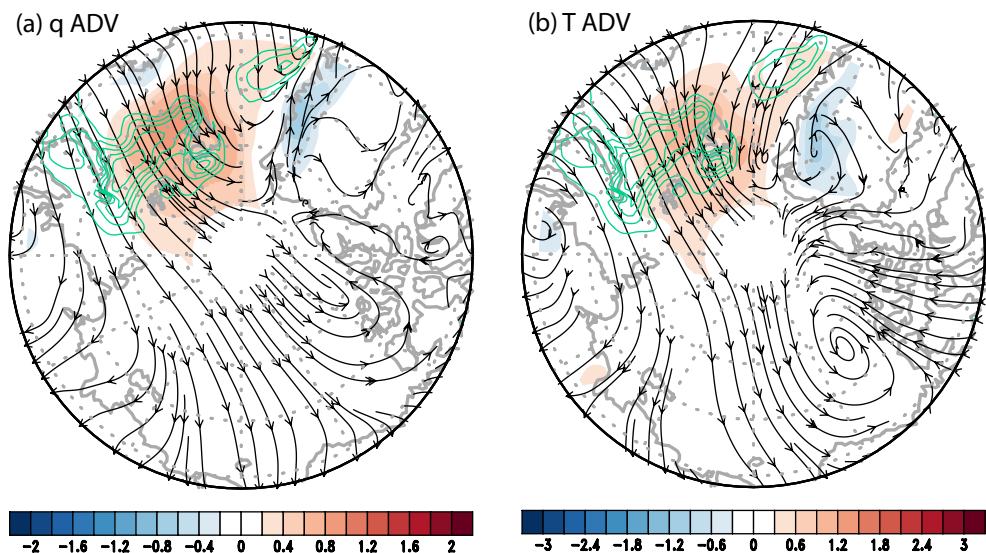


**Figure 4.2.** Winter-averaged (a) moisture transport (*streamline*) and its convergence (*shading*), and (b) heat transport (*streamline*) and its convergence (*shading*) in the lower troposphere (1000–850 hPa) associated with the sea ice loss mode. The green contours represent the reduction of sea ice concentration.

## 4.1 Moisture budget

In order to assess the relative role of horizontal and vertical processes in the Arctic warming, let us first consider the following moisture conservation equation in pressure coordinates:

$$\frac{\partial q}{\partial t} = -\bar{u} \cdot \nabla q + S = -\bar{u} \cdot \nabla_p q - \omega \frac{\partial q}{\partial p} + S, \quad (16)$$

where  $q$  is specific humidity,  $\bar{u}$  is velocity,  $p$  is pressure,  $\omega \equiv Dp/Dt$  is “omega” vertical velocity,  $S$  is moisture source, and the subscript  $p$  denotes that differentiation is on a constant pressure surface. If we multiply (16) by  $\rho_a$  and integrate the resulting equation with respect to  $z$ , we obtain

$$\frac{\partial}{\partial t} \int_0^z \rho_a q dz = - \int_0^z \rho_a \bar{u} \cdot \nabla_p q dz - \int_0^z \rho_a \omega \frac{\partial q}{\partial p} dz + \rho_w (E - P), \quad (17)$$

where  $\rho_a$  is density of air,  $\rho_w$  is density of water, and the moisture source is equal to evaporation ( $E$ ) minus precipitation ( $P$ ). Equation (17) can be rewritten as

$$\int_p^{p_0} \Delta q dp = \left[ - \int_p^{p_0} \bar{u} \cdot \nabla_p q dp - \int_p^{p_0} \omega \frac{\partial q}{\partial p} dp + \rho_w g (E - P) \right] \Delta t, \quad (18)$$

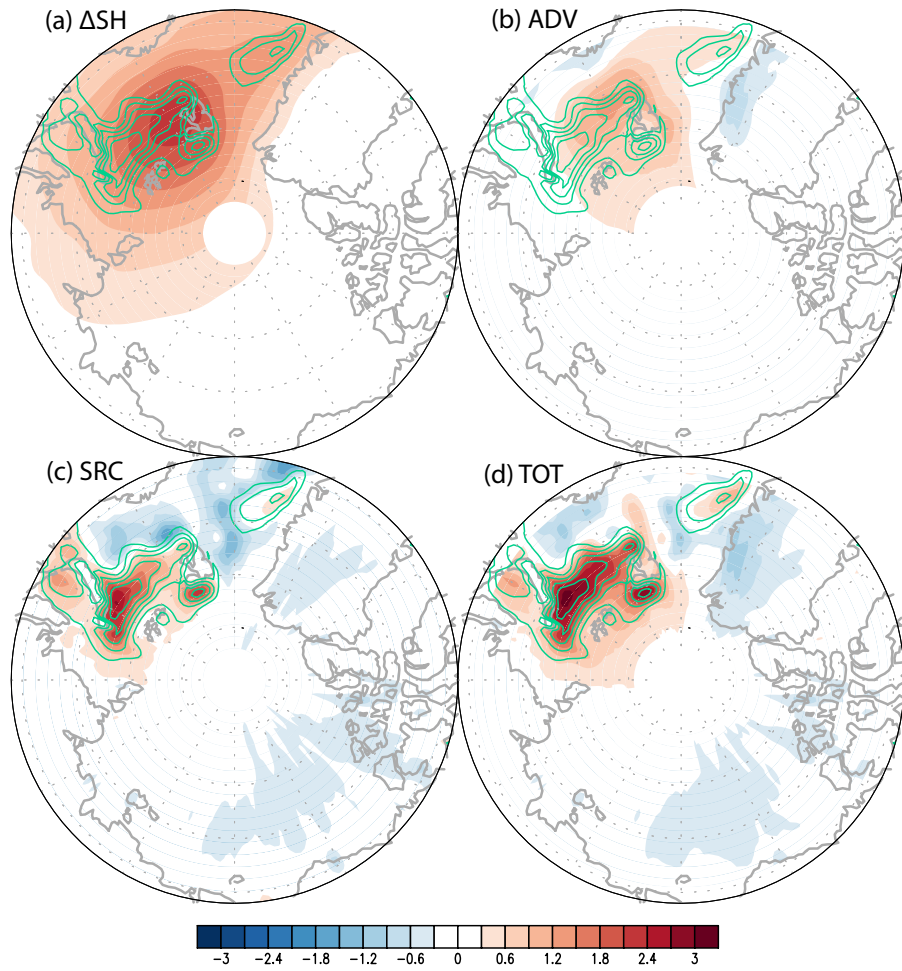
where  $g$  is gravitational acceleration,  $p = p(z)$ , and  $p_0$  is surface pressure which is assumed to be 1000 hPa here. The right-hand side is the total amount of moisture change due respectively to horizontal advection, vertical convection and net evaporation (evaporation minus precipitation) during a time interval  $\Delta t$ , which is one day in the present study. The left-hand side, then, is the amount of moisture increase (anomalous specific humidity) in the atmospheric column.

Regression analysis is conducted in CSEOF space on all variables in (18) so that their spatio-temporal evolutions become consistent with the evolution of sea ice in Fig. 3.1b. Then, the regressed CSEOF loading vectors are used to evaluate each term in (18) in order to assess quantitatively the importance of each term in explaining the changes in specific humidity in association with the sea ice reduction over the Barents-Kara Seas.

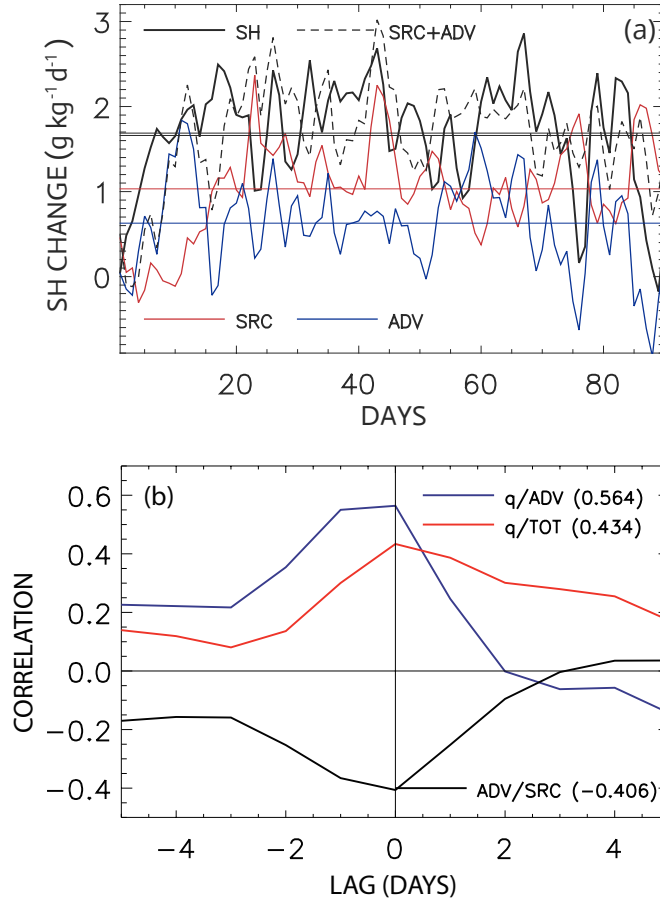
The spatial and temporal patterns of specific humidity, horizontal advection and vertical source terms in (18), in association with the sea ice reduction in Fig. 3.1b, are summarized in Figs. 4.3, 4.4 and Table 4.1. The winter-averaged regressed pattern of lower-tropospheric (1000–850 hPa) specific humidity (Fig. 4.3a) is depicted together with the contributions from the horizontal advection (Fig. 4.3b), source (evaporation minus precipitation; Fig. 4.3c), and the sum of all contributions (right-hand side of (18); Fig. 4.3d). The contribution from the vertical convection of moisture is very small in the lower troposphere (Table 4.1). As can be seen, the magnitude of moistening from the source term is comparatively larger than the horizontal advection of moisture in association with Arctic amplification. Both the local source (net evaporation) and the horizontal advection of moisture seem essential in explaining the increased specific humidity in the atmospheric column.

Figure 4.4 shows the daily time series of the terms in (18) averaged over the region of sea ice reduction (boxed area in Fig. 3.1a), and the correlations among the individual terms. As can be seen, the net increase in specific humidity in the lower troposphere (1000–850 hPa), on average, is  $\sim 1.7 \text{ g kg}^{-1}$  (black line) during winter due to sea ice loss. This amount is roughly explained by adding source term ( $\sim 1 \text{ g kg}^{-1}$ ; red line) and horizontal moisture transport ( $\sim 0.6 \text{ g kg}^{-1}$ ;

<sup>1</sup>; blue line). Thus, the vertical process plays a stronger role in the net increase of specific humidity in association with Arctic amplification. On the other hand, horizontal moisture transport is significantly correlated with the variation of specific humidity; maximum correlation is 0.564 at lag zero (Fig. 4.4b and Table 4.1). Thus, the variability of specific humidity (not the mean) is strongly controlled by the horizontal advection of moisture. During advection of dry air, net evaporation is increased and vice versa as indicated by the negative correlation between the moisture advection and source terms; correlation is about -0.406 (Fig. 4.4b and Table 4.1). Thus, the source term tends to moderate the effect of horizontal advection of moisture over the Barents-Kara Seas.



**Figure 4.3.** The winter-averaged lower tropospheric (1000–850 hPa) patterns of variables: (a) specific humidity, (b) moisture advection, (c) moisture source (evaporation minus precipitation), and (d) total (horizontal plus vertical) moisture supply. All the terms are converted into specific humidity ( $\text{g kg}^{-1}$ ).



**Figure 4.4.** (a) Daily fluctuation of 1000–850 hPa averaged specific humidity (SH), evaporation minus precipitation (SRC), and horizontal moisture transport (ADV) averaged over the region of sea ice reduction ( $21^{\circ}$ – $79.5^{\circ}\text{E}$ ,  $75^{\circ}$ – $79.5^{\circ}\text{N}$ ) in the Barents-Kara Seas (boxed area in Fig. 3.1a). The straight lines represent the winter means of individual variables. (b) Lagged correlation between specific humidity and horizontal moisture transport (*blue*), between the horizontal transport and source (evaporation minus precipitation) (*black*), and between the specific humidity and the total (source plus advection) (*red*).



**Table 4.1.** Statistics of the lower tropospheric (1000–850 hPa) winter moisture budget averaged over the region of sea ice reduction (21°–79.5°E, 75°–79.5°N) in the Barents-Kara Seas: SH is specific humidity, H ADV is horizontal advection of moisture, SRC is source (evaporation minus precipitation), V CNV is vertical convection, TOT is sum of advection, source and convection terms, and ERR is the difference between specific humidity and TOT.

Term	Mean [g kg <sup>-1</sup> d <sup>-1</sup> ]	Ratio to $\Delta q$ [%]	Std. dev. [g kg <sup>-1</sup> d <sup>-1</sup> ]	Corr. with $\Delta q$ [ - ]
SH ( $\Delta q$ )	1.684	–	0.646	–
H ADV	0.603	35.8	0.555	0.564
SRC ( $E-P$ )	1.032	61.3	0.564	–0.087
V CNV	0.091	5.4	0.109	0.587
TOT	1.726	102.5	0.650	0.434
ERR ( $\Delta q$ -TOT )	–0.042	–2.5	0.637	–

## 4.2. Thermal energy budget

Let us now consider the thermal energy equation:

$$\frac{\partial T}{\partial t} + \vec{u} \cdot \nabla_p T - S_p \omega = \frac{J}{c_p}, \quad (19)$$

where the stability parameter  $S_p$  is defined by

$$S_p = \frac{RT}{c_p p} - \frac{\partial T}{\partial p} = -\frac{T}{\theta} \frac{\partial \theta}{\partial p}. \quad (20)$$

Here  $c_p$  is the specific heat at constant pressure,  $R$  is the specific gas constant,  $\theta$  is potential temperature, and  $J$  is diabatic forcing (heat flux per unit volume). If we integrate (19) with respect to  $p$ , we have

$$\int_p^{p_0} \Delta T dp = \left[ - \int_p^{p_0} \vec{u} \cdot \nabla_p T dp + \int_p^{p_0} S_p \omega dp + \int_p^{p_0} \frac{J}{c_p} dp \right] \Delta t. \quad (21)$$

The diabatic forcing includes latent and sensible heat flux at the surface as well as radiative forcing in the atmospheric column produced by the increased specific humidity. Thus, we assume that the last term can be written as

$$\int_0^{p_0} \frac{J}{c_p} dp = \frac{g}{c_p} (F_S + F_L + F_R), \quad (22)$$

where  $F_S$ ,  $F_L$  and  $F_R$  are sensible heat flux, latent heat flux, and radiative flux, respectively. The radiative flux in the entire atmospheric column is determined by the net radiation trapped in the atmospheric column, i.e.,

$$F_R = F_{\text{surface}} - F_{\text{TOA}}. \quad (23)$$

Figure 4.5 shows the total greenhouse effect produced by the increased specific humidity. Here, the greenhouse effect is expressed as the net increase in radiative forcing in the atmospheric column, which is primarily due to the increased specific humidity. As can be seen in Fig. 4.5b, there is a strong correlation (0.7) between the variability of specific humidity and that of greenhouse effect over the region of sea ice reduction. Over the Barents-Kara Seas, radiative forcing increased by more than  $30 \text{ W m}^{-2}$  during the last 40 years; this area-averaged value is obtained by multiplying the loading vector (Fig. 4.5a) with the PC time series (Fig. 3.1c). Thus, the increased moisture is one of important reasons for atmospheric warming associated with Arctic amplification.

The ERA-Interim reanalysis products provide longwave radiation only at the surface and the top of the atmosphere. In order to evaluate the greenhouse effect within a vertical layer, it is assumed that the greenhouse effect is proportional to the anomalous specific humidity in the vertical column (see Fig. 4.6). This assumption is partly based on the high correlation between the two variables (Fig. 4.5b), but is an important caveat in the present study. As can be seen in Figs. 4.1c and 4.1d, increase in specific humidity is mainly confined to the lower troposphere (see also Fig. 4.6). Therefore, heating due to greenhouse effect should be most conspicuous in the lower troposphere. As seen in Figs. 4.1a and 4.1b, atmospheric warming is also most conspicuous in the lower troposphere. In calculating the contribution from the greenhouse effect to atmospheric warming, we assume that  $\sim 63\%$  of moisture increase is from the vertical source and  $\sim 37\%$  from the horizontal advection. When the

relative roles of vertical source and horizontal advection are estimated, this percentage is taken into account.

Like the moisture budget case, the regressed CSEOF loading vectors are used to evaluate each term in (21) in order to assess the importance of each term in explaining the changes in temperature in association with the sea ice reduction. Figure 4.7 shows the terms on the right-hand side of (21). The pattern of the turbulent heat flux indicates that it is strongly tied with the reduction of sea ice in the Barents-Kara Seas. The horizontal heat transport and greenhouse effect seem similar in magnitude but are not strictly confined to the region of sea ice reduction. The addition of these three terms and the vertical convection term, which is much smaller than the others (Table 4.2), yields the total forcing (converted into temperature) in Fig. 4.7a. The total forcing term is fairly similar, both in terms of the pattern and magnitude, to the lower-tropospheric temperature increase (Fig. 4.8).

Figure 4.9a shows the daily variation of temperature and the heating terms in (21) converted into temperatures averaged over the region of sea ice reduction (see Fig. 3.1a). As can be seen in Fig. 4.9 and Table 4.2, the lower tropospheric temperature increased by  $\sim 2.15$  K during DJF over the region of sea ice reduction. A little more than 1.20 K is explained by the turbulent heat flux (0.69 K) plus 63% of the greenhouse effect due to increased moisture (0.51 K). The horizontal advection explains 0.62 K increase in the lower tropospheric temperature plus 37% of the greenhouse effect (0.30 K).

The lagged correlation shows that there is a significant positive correlation between the tropospheric temperature and the heat advection (Fig.

4.9b). During a cold advection, tropospheric temperature decreases and vice versa. It is also apparent that turbulent heat flux increases during a cold advection and vice versa as indicated by the negative correlation ( $-0.552$ ) at lag zero. As can be seen in Fig. 4.9b and Table 4.2, the sum of turbulent heat flux and greenhouse effect has the negative correlation with the tropospheric temperature even though the greenhouse effect correlates with the tropospheric temperature positively because the variation of the turbulent heat flux is larger than that of the greenhouse effect. Thus, the turbulent heat flux tends to moderate the effect of thermal advection over the region of sea ice reduction. This compensation accomplished by turbulent heat flux, however, is small compared with the thermal advection itself. As a result, the total heating (turbulent heat flux + horizontal heat transport + greenhouse effect) is still positively correlated with the tropospheric temperature. Thus, the horizontal advection of heat is critical in explaining the variability (not the mean) of the tropospheric temperature in association with Arctic amplification. On the other hand, the turbulent flux term, the advection term, and the greenhouse effect make nearly equal contributions to the net atmospheric warming over the Barents-Kara Seas. All three terms are needed to explain  $\sim 99\%$  ( $\sim 2.12$  K) of the lower tropospheric warming.

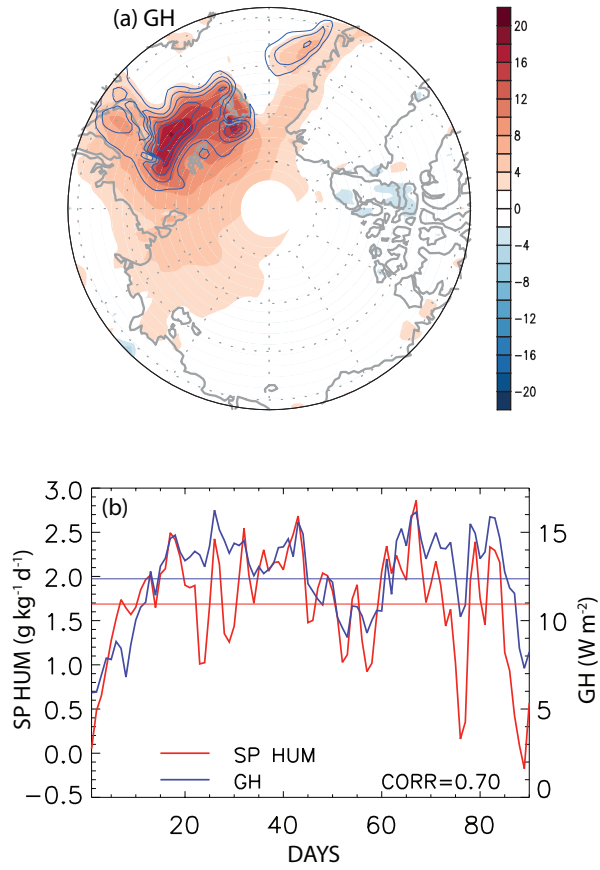


**Figure 4.5.** (a) The winter-averaged spatial pattern of the greenhouse effect ( $\text{W m}^{-2}$ ). (b) The daily variation of specific humidity (*red*) in the lower troposphere (1000–850 hPa) and the greenhouse effect (*blue*) averaged over the region of sea ice reduction ( $21^{\circ}$ – $79.5^{\circ}\text{E} \times 75^{\circ}$ – $79.5^{\circ}\text{N}$ ) in the Barents-Kara Seas.

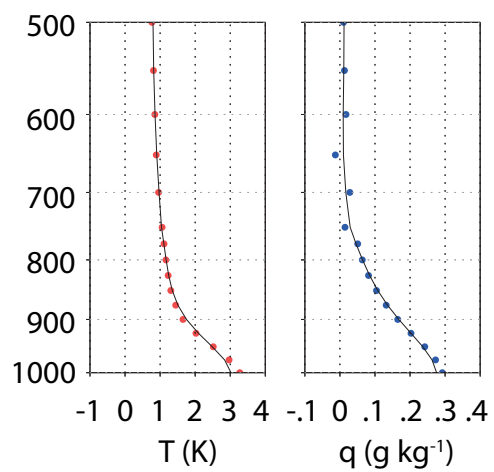


**Figure 4.6.** The vertical profile of anomalous temperature and specific humidity over the region of sea ice reduction ( $21^{\circ}$ – $79.5^{\circ}$ E  $\times$   $75^{\circ}$ – $79.5^{\circ}$ N) in the Barents-Kara Seas.

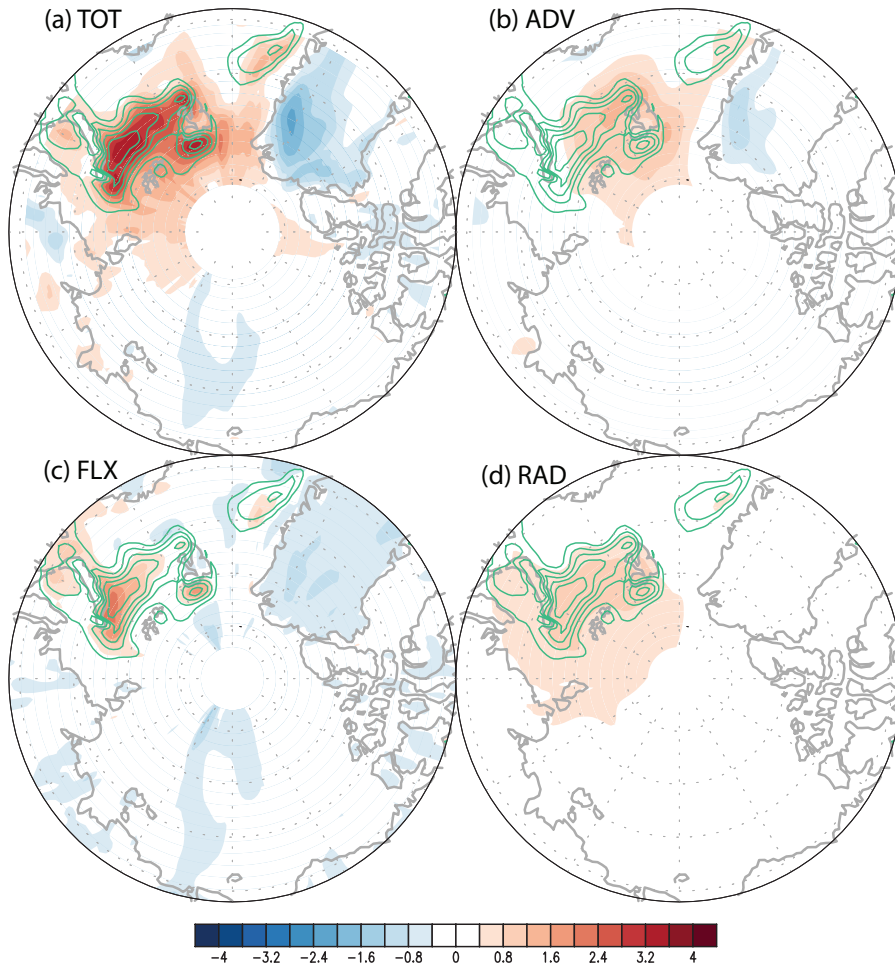


**Figure 4.7.** The winter-averaged lower-tropospheric (1000–850 hPa) patterns of (a) total heat, (b) heat transport, (c) turbulent (sensible + latent) heat flux, and (d) greenhouse effect. All the terms are converted into temperature anomalies (K).



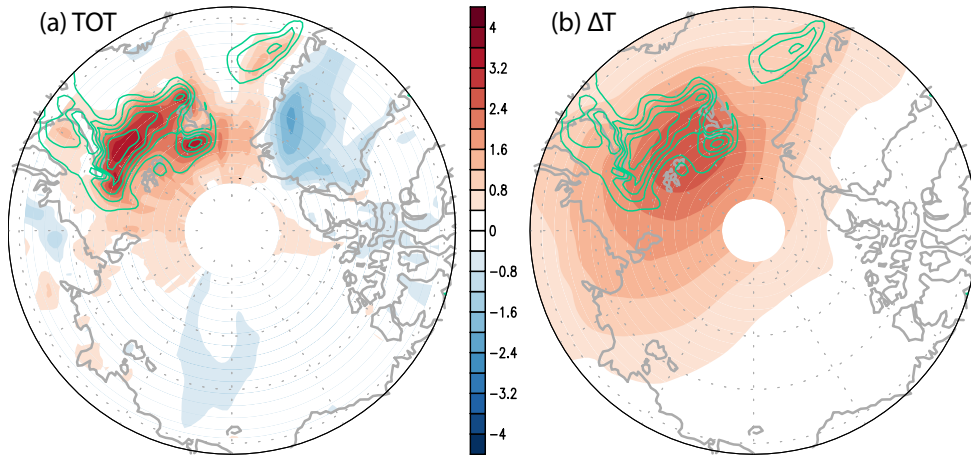


**Figure 4.8.** The winter averaged lower tropospheric (1000–850 hPa) patterns of (a) total heating converted into temperature, and (b) atmospheric temperature.

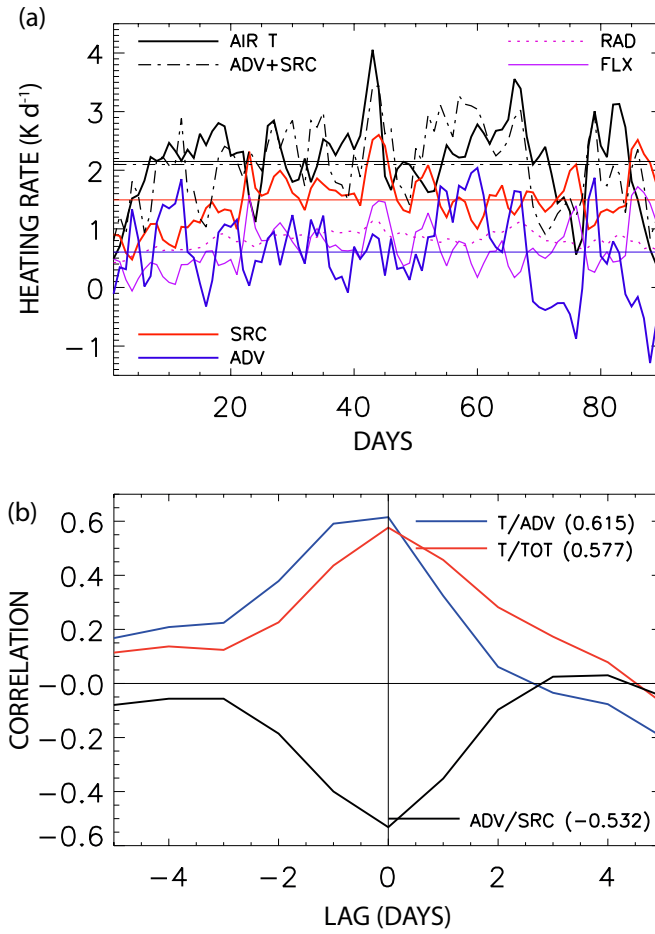


**Figure 4.9.** (a) Daily fluctuation of 1000–850 hPa averaged temperature (AIR T), turbulent flux (FLX), radiation (RAD), and horizontal heat transport (ADV). The thick red curve is the sum of turbulent flux and radiation (SRC). The straight lines represent the winter means of individual variables. (b) Lagged correlation between temperature and horizontal transport (*blue*), between the horizontal transport and the other source terms (*black*), and between the temperature and the total energy (*red*).

**Table 4.2.** Statistics of the lower tropospheric (1000–850 hPa) winter heat budget averaged over the region of sea ice reduction (21°–79.5°E, 75°–79.5°N) in the Barents-Kara Seas: AIR T is atmospheric temperature, H ADV is horizontal advection of heat, FLX is turbulent heat flux, RAD is greenhouse effect, V CNV is vertical convection, TOT is sum of all contributions, and ERR is the difference between air temperature and TOT.

Term	Mean [K d <sup>-1</sup> ]	Ratio to $\Delta T$ [%]	Std. dev. [K d <sup>-1</sup> ]	Corr. with $\Delta T$ [ - ]
AIR T ( $\Delta T$ )	2.149	–	0.698	–
H ADV	0.623	29.0	0.600	0.615
FLX	0.685	31.9	0.391	–0.304
RAD	0.809	37.6	0.104	0.680
V CNV	0.020	0.9	0.353	0.080
TOT	2.137	99.4	0.665	0.577
ERR ( $\Delta T$ –TOT)	0.012	0.6	0.665	–

### 4.3. Moist static energy budget

Moist static energy is defined by

$$m = c_p T + gz + L_e q, \quad (24)$$

where  $c_p$  ( $=1004 \text{ J kg}^{-1} \text{ K}^{-1}$ ) is specific heat at constant pressure,  $T$  is temperature (K),  $g$  ( $=9.8 \text{ m s}^{-2}$ ) is gravitational acceleration,  $z$  (m) is elevation,  $L_e$  ( $=2265 \times 10^3 \text{ J kg}^{-1}$ ) is latent heat of evaporation, and  $q$  ( $\text{kg kg}^{-1}$ ) is specific humidity. Thus, the unit of moist static energy is  $\text{J kg}^{-1}$ . Change in moist static energy, therefore, is written as

$$dm = c_p dT + g dz + L_e dq = c_p dT + d\Phi + L_e dq, \quad (25)$$

where  $\Phi$  is geopotential. Then, CSLV of moist static energy can be determined from CSLVs of air temperature, geopotential, and specific humidity. Figure 4.10 shows the winter-averaged regressed pattern of moist static energy derived from the regressed pattern of air temperature, geopotential and specific humidity according to (25). As can be seen, moist static energy has increased significantly over the region of sea ice reduction.

The vertically integrated budget equation for the moist static energy is written as (Maloney, 2009)

$$\int_0^z \rho_a \frac{\partial m}{\partial t} dz + \int_0^z \rho_a \bar{u} \cdot \nabla_p m dz + \int_0^z \rho_a \omega \frac{\partial m}{\partial p} dz = \text{SH} + \text{LH} + \text{LW} + \text{SW}, \quad (26)$$

where SH is sensible heat flux, LH is latent heat flux, LW is longwave radiative forcing, and SW is shortwave radiative forcing. The right-hand side of (26) represents the source term including turbulent heat flux entering the

atmosphere and net radiative forcing in the atmospheric column. The unit of the terms in (26) is  $\text{W m}^{-2}$ . Note that (26) is essentially the sum of the heat equation and the moisture equation scaled respectively by  $c_p$  and  $L_e$  (chapter 4.1 and 4.2) except that potential energy ( $d\Phi$ ) is added to the left-hand side of (26). It should be noted that LW includes the greenhouse effect in association with changes in specific humidity. Equation (26) can be rewritten as

$$\int_p^{p_0} \Delta m dp = \left[ - \int_p^{p_0} \vec{u} \cdot \nabla_p m dp - \int_p^{p_0} \omega \frac{\partial m}{\partial p} dp + g(\text{SH} + \text{LH} + \text{LW} + \text{SW}) \right] \Delta t. \quad (27)$$

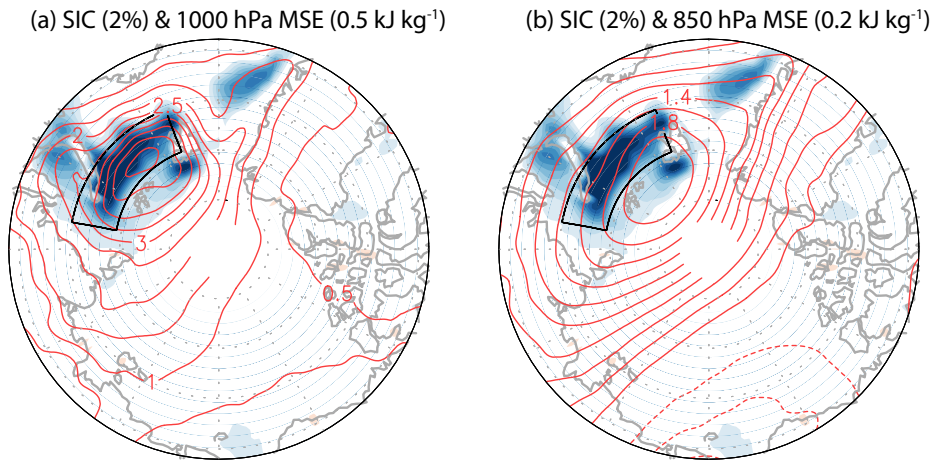
Thus, change in moist static energy (left-hand side) is due to advection (first term on the right-hand side), convection (second term), and source (the terms in parenthesis) of moist static energy.

Figure 4.11 shows the winter-averaged advection term, flux term, radiation term, and the right-hand side of (27), all scaled by  $c_p(p_0 - p)$  to convert them into daily mean temperature change averaged over 1000–850 hPa vertical column. As can be seen, the flux term increases significantly over the region of sea ice reduction. The radiation term also increases over the region of sea ice reduction although radiational heating is also seen away from the source region. The advection term is seen mainly on the Atlantic side of the sea ice reduction. These three terms on the right-hand side of (27) are reasonably similar in magnitude.

Figure 4.12 shows the winter-averaged moist static energy increases (left-hand side of (27)) and the total heating term (right-hand side of (27)). As can be seen, both terms are significant over the region of sea ice reduction. The

total term (Fig. 4.12b) looks similar in magnitude and pattern to the moist static energy increase (Fig. 4.12a).

Figure 4.13a shows the daily variation of each term in (27) averaged over the region of sea ice reduction. As can be seen, advection, heat flux, and radiative forcing make nearly equal contributions to changes in moist static energy over the region of sea ice loss. Figure 4.13b further shows lagged correlations among the daily variation of moist static energy, horizontal advection, vertical heat flux, and total heating term as defined in (27) averaged over the Barents-Kara Seas. Variation of moist static energy is strongly correlated with both the advection term ( $\text{corr}=0.640$ ) and the total heating term ( $\text{corr}=0.593$ ). Heat flux term is negatively correlated ( $\text{corr}=-0.526$ ) with the advection term, implying that positive advection of moist static energy decreases vertical heat flux and vice versa.



**Figure 4.10.** The winter-averaged regressed pattern of moist static energy (*contours*) at (a) 1000 hPa and (b) 850 hPa on top of sea ice anomaly pattern (*shading*).

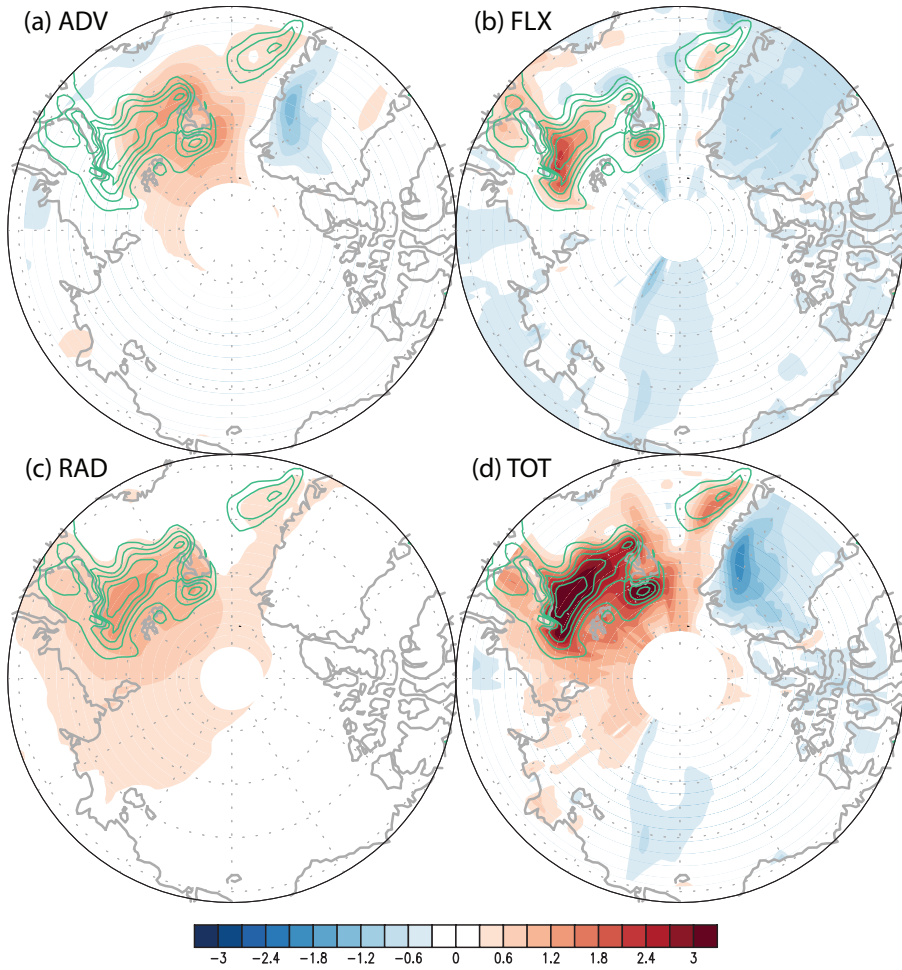


**Figure 4.11.** Winter-averaged pattern of 1000–850 hPa daily (a) advection, (b) flux, (c) radiation, and (d) total (right-hand side of (27)). All quantities are scaled by  $c_p(p_0 - p)$ .



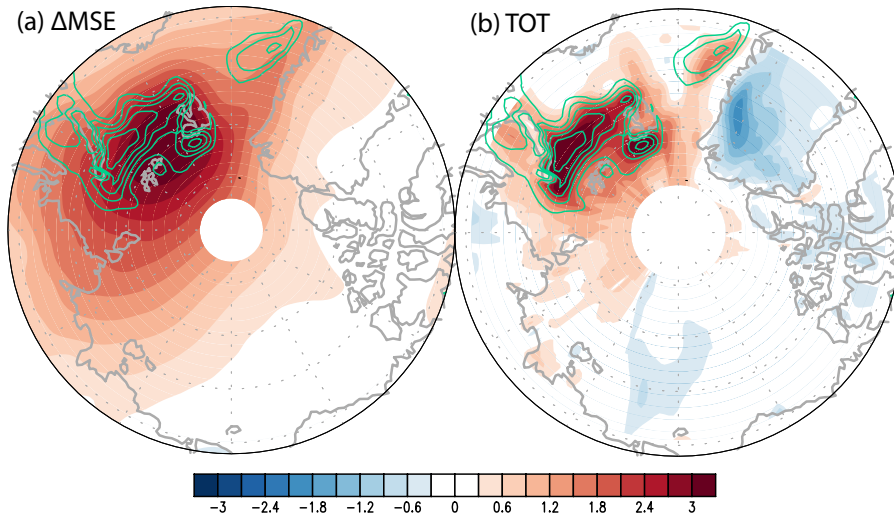


**Figure 4.12.** Winter-averaged pattern of 1000–850 hPa daily (a) moist static energy and (b) total heating term (right-hand side of (27)). All quantities are scaled by  $c_p(p_0 - p)$ .

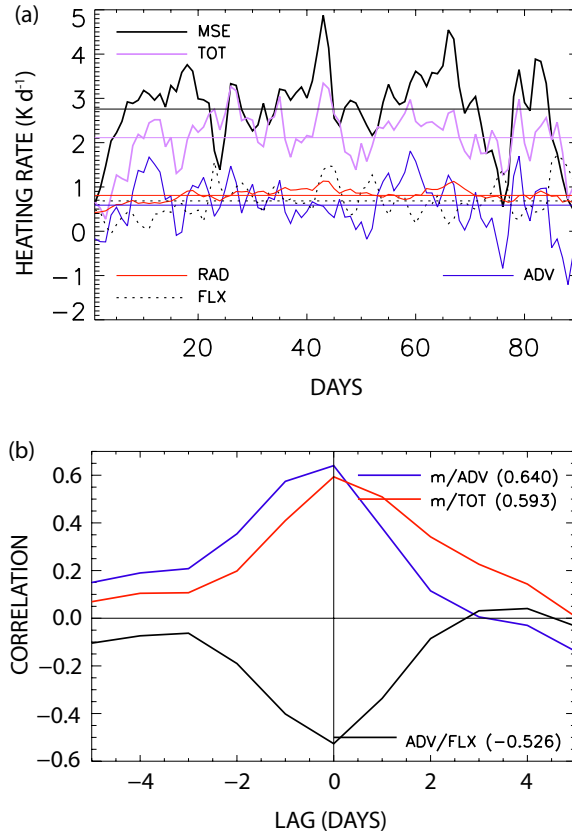


**Figure 4.13.** (a) Daily fluctuation of 1000–850 hPa averaged moist static energy (MSE), turbulent flux (FLX), radiation (RAD), horizontal advection of moist static energy (ADV), and sum of all contributions (TOT). The straight lines represent the winter means of individual variables. (b) Lagged correlation between moist static energy (*m*) and horizontal advection (*blue*) and total heating term (*red*), and between horizontal advection and flux (*black*).

#### 4.4. Sensitivity test on the level of closure

So far, the upper level of significant change in specific humidity and air temperature is chosen to be  $p = 850$  hPa based on Fig. 4.1 (see also the vertical profile of anomalous temperature and specific humidity in Fig. 4.6). The conspicuous warming signal is in the lower troposphere below approximately 700 hPa and two different choices ( $p = 900$  and  $p = 750$  hPa) of the upper level of integration are also tested. Results by using two different upper pressure levels ( $p = 900$  and  $p = 750$  hPa) are shown in Figs. 4.14–4.19. Figure 4.14 and 4.15 show the results of the moisture budget analysis using two different upper levels, Figure 4.16 and 4.17 show the same but for the thermal energy budget. All results are summarized in Fig. 4.19.

Difference in relative contributions of the terms in the moisture and heat budget equations becomes gradually smaller as the level of the upper boundary increases. This is an expected result, since contribution from the vertical processes generally decreases with elevation, whereas contribution from the horizontal processes may not necessarily decrease with elevation. However, the level of closure for heat and moisture budget equations does not seriously alter the relative importance of the terms in the budget equation, and the conclusion in the previous section does not change in any substantial manner when a reasonable upper pressure levels ( $p$ ) is used for calculating the energy budget. This sensitivity test indicates that the relative importance of the vertical processes to horizontal advective processes increases as the elevation decreases (see also Fig. 4.6).

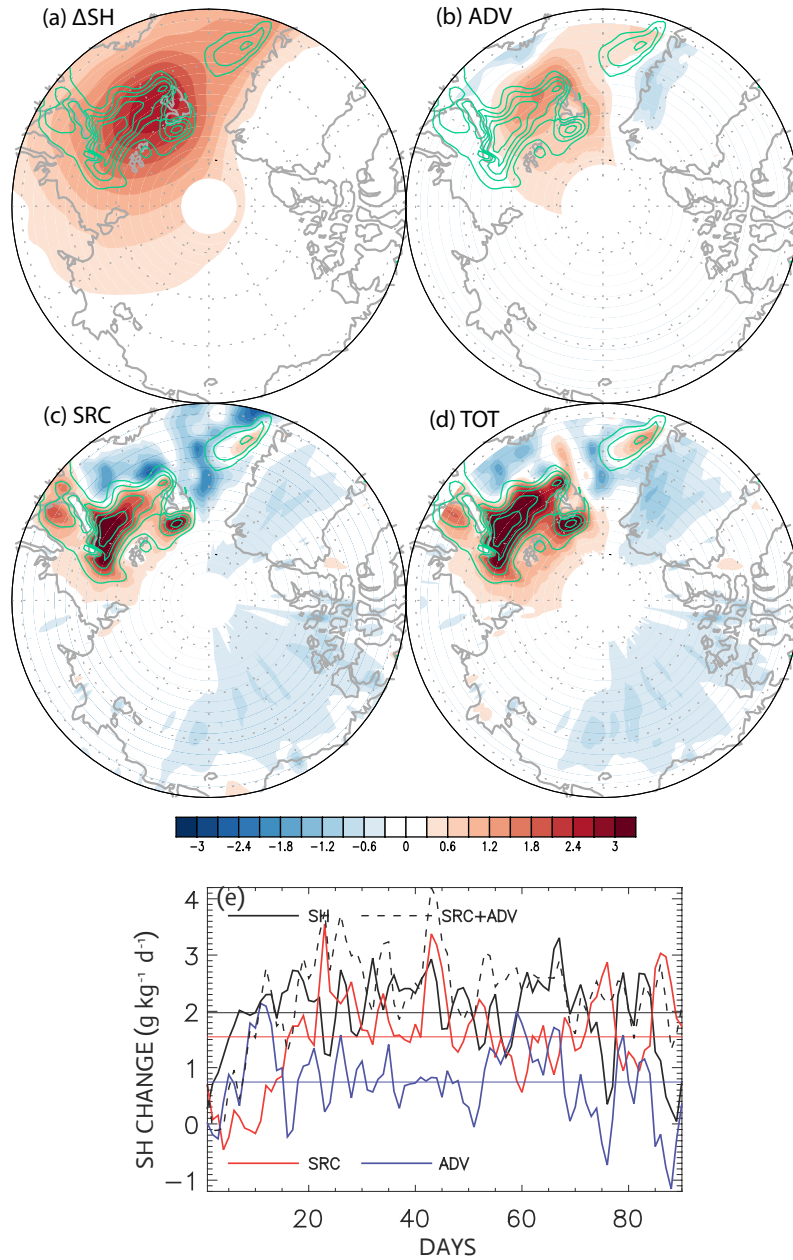


**Figure 4.14.** The winter-averaged lower tropospheric (1000–900 hPa) patterns of variables: (a) specific humidity, (b) moisture transport, (c) moisture source (evaporation – precipitation), and (d) total (horizontal plus vertical) moisture source. All the source terms are converted into specific humidity ( $g\ kg^{-1}$ ). (e) Daily fluctuation of 1000–900 hPa averaged specific humidity (SH), evaporation minus precipitation (SRC), and horizontal moisture transport (ADV) averaged over the region of sea ice reduction ( $21^{\circ}$ – $79.5^{\circ}E$ ,  $75^{\circ}$ – $79.5^{\circ}N$ ) in the Barents-Kara Seas (boxed area in Fig. 3.1a). The straight lines represent the winter means of individual variables.

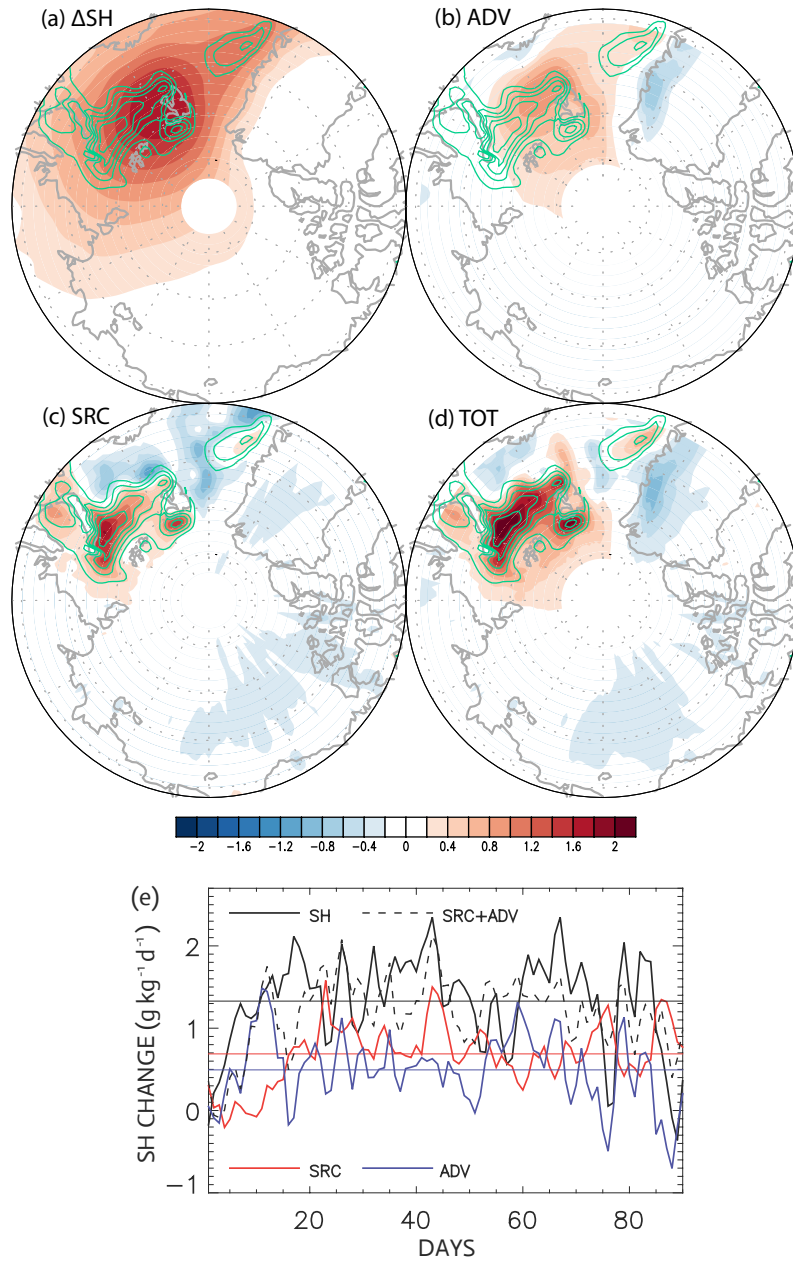


**Figure 4.15.** The winter-averaged lower tropospheric (1000–750 hPa) patterns of variables: (a) specific humidity, (b) moisture transport, (c) moisture source (evaporation – precipitation), and (d) total (horizontal plus vertical) moisture source. All the source terms are converted into specific humidity ( $g\ kg^{-1}$ ). (e) Daily fluctuation of 1000–750 hPa averaged specific humidity (SH), evaporation minus precipitation (SRC), and horizontal moisture transport (ADV) averaged over the region of sea ice reduction ( $21^{\circ}$ – $79.5^{\circ}E$ ,  $75^{\circ}$ – $79.5^{\circ}N$ ) in the Barents-Kara Seas (boxed area in Fig. 3.1a). The straight lines represent the winter means of individual variables.

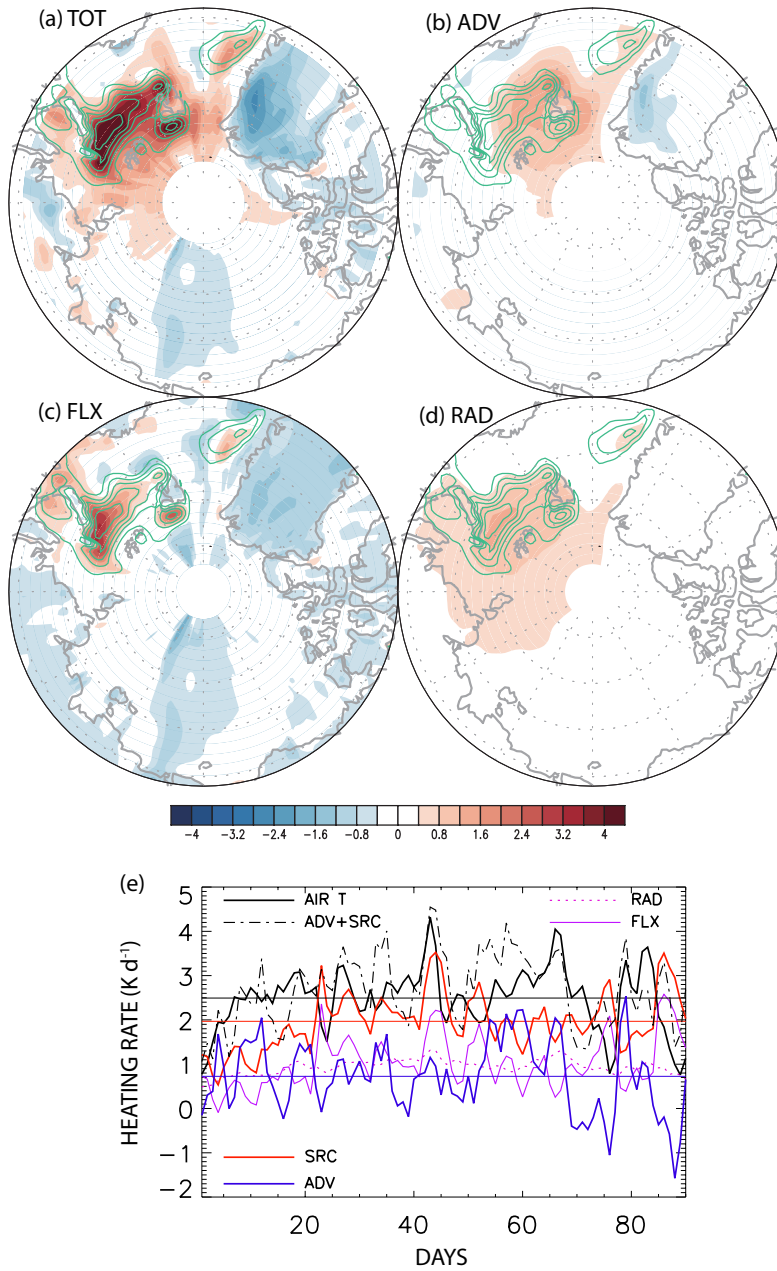


**Figure 4.16.** The winter-averaged lower-tropospheric (1000–900 hPa) patterns of (a) total heat, (b) heat transport, (c) turbulent (sensible + latent) heat flux, and (d) greenhouse effect. All the terms are converted into temperature anomalies (K). (e) Daily fluctuation of 1000–900 hPa averaged temperature (AIR T), turbulent flux (FLX), radiation (RAD), and horizontal heat transport (ADV). The thick red curve is the sum of turbulent flux and radiation (SRC). The straight lines represent the winter means of individual variables.

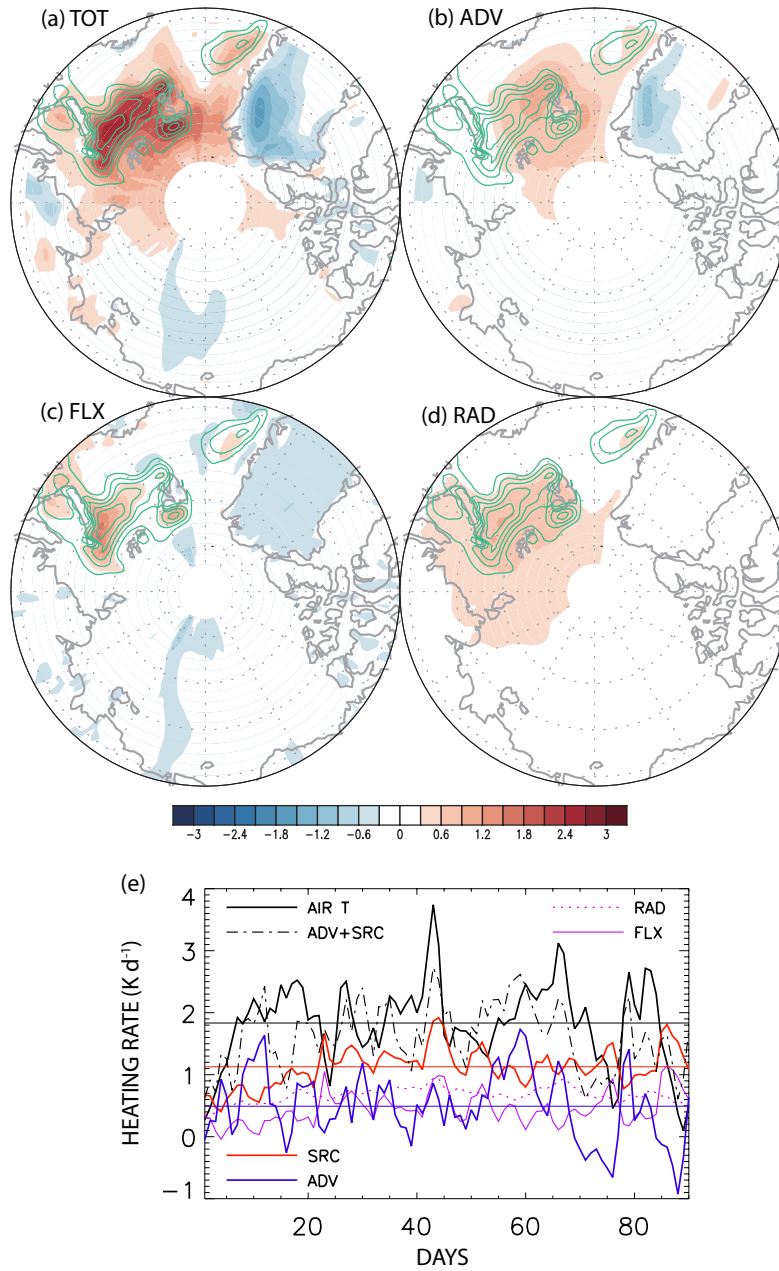


**Figure 4.17.** The winter-averaged lower-tropospheric (1000–750 hPa) patterns of (a) total heat, (b) heat transport, (c) turbulent (sensible + latent) heat flux, and (d) greenhouse effect. All the terms are converted into temperature anomalies (K). (e) Daily fluctuation of 1000–750 hPa averaged temperature (AIR T), turbulent flux (FLX), radiation (RAD), and horizontal heat transport (ADV). The thick red curve is the sum of turbulent flux and radiation (SRC). The straight lines represent the winter means of individual variables.



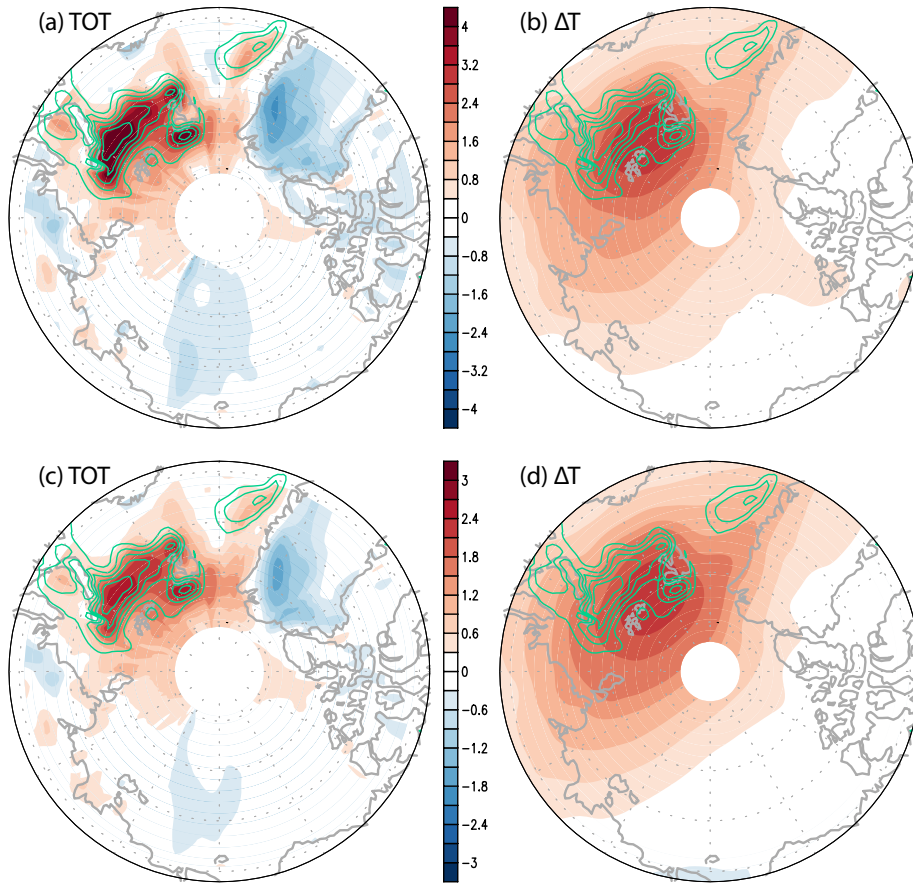


**Figure 4.18.** (upper panel) The winter averaged lower tropospheric (1000–900 hPa) patterns of (a) total heating converted into temperature, and (b) atmospheric temperature. (lower panel) The same as the upper panel except for the pressure level of 1000–750 hPa.



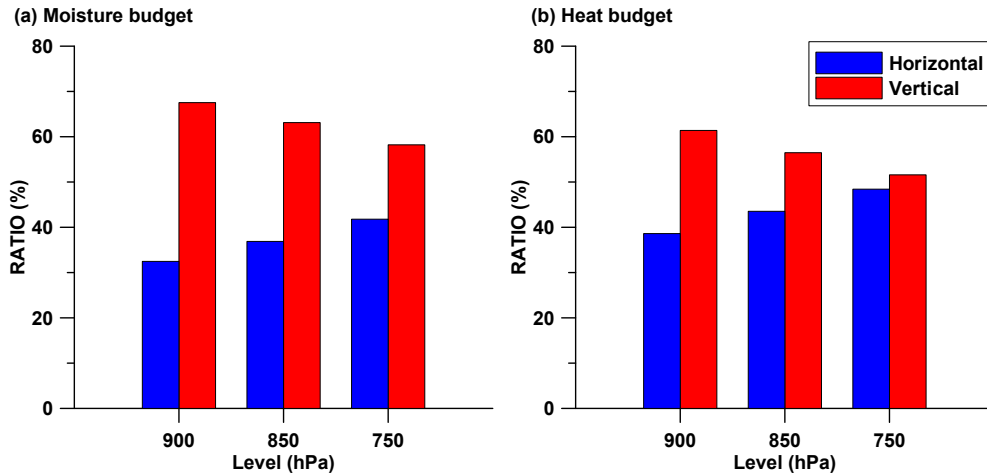


**Figure 4.19.** Contributions of the horizontal and vertical processes to (a) moisture increase and (b) air temperature increase according to the level of budget closure in the lower troposphere. In (a; moisture budget case), horizontal moisture advection and moisture source (evaporation minus precipitation) are compared. In (b; heat budget case), horizontal heat advection and greenhouse effect induced by horizontal moisture advection is compared against the sum of turbulent heat flux and greenhouse effect induced by moisture source in the heat budget equation.

## Chapter 5. Concluding Remarks

Based on the daily ERA-Interim reanalysis data, detailed changes in the sea ice and other key variables in the Barents and Kara Seas are examined in order to understand the mechanism of winter Arctic amplification. A quantitative estimation of the sea ice-induced changes reveals that increase in downward longwave radiation is sustained by an increase in turbulent flux from sea surface exposed to air due to sea ice reduction. While a wider area of sea surface is exposed to air and upward longwave radiation increases due to summer sea surface warming, the increased upward longwave radiation alone seems insufficient to produce a feedback loop. Due to a net deficit of surface radiation in fall/winter, sea ice may refreeze quickly (see Figs. 7 and 8 in Kim et al., 2016). Prolonged sea ice reduction is instrumental for increased turbulent flux, which in turn warms the atmospheric column (see Fig. 3.5). As a result, downward longwave radiation increases and sea ice reduction continues in accordance with surface warming (Fig. 3.7). This is why significant Arctic amplification is observed only in the Barents and Kara Seas but not in the Laptev, East Siberian or Chukchi Seas, where summer sea ice melting is conspicuous but sea ice quickly refreezes in late fall/early winter (Kim et al., 2016). How sea ice refreezing is delayed in the Barents and Kara Seas remains to be answered. Sea ice cover in the Barents and Kara Seas was  $\sim 80\%$  in 1979 and is currently  $\sim 40\%$ . An exponential curve is fitted to the amplitude time series of the sea ice loss mode (Fig. 3.1d); an exponential fitting is chosen, since it minimizes the residual error. According to the exponential fitting, the amplitude of sea ice reduction and atmospheric warming increases at the rate of  $\sim 8.9\%$  every year.

It should be pointed out that this feedback process could develop in other areas of the Arctic Ocean. If sea ice refreezing is delayed in late fall/winter, increased turbulent heat flux from the open sea surface will make it more difficult for sea surface to refreeze, ultimately leading to the feedback process in Fig. 3.13. It is, of course, difficult to determine when this should occur, since environmental factors differ from one location to another.

Detailed heat and moisture budgets are examined in association with Arctic amplification in order to delineate the relative roles of horizontal and vertical processes. The conspicuous warming signal is in the lower troposphere below approximately 700 hPa. Therefore, the analysis results are shown primarily for the lower troposphere (1000–850 hPa).

The moisture budget indicates that about 60% of the increased moisture derives from the increased evaporation from the region of sea ice reduction. The pattern of evaporation minus precipitation looks fairly similar to the pattern of sea ice reduction. The bulk of the remaining 40% is explained by the horizontal moisture advection. While the latter is less effective in explaining the increased specific humidity, it is the primary source of variability of specific humidity in the lower troposphere. The moisture advection is strongly correlated with the variability of the specific humidity over the Barents-Kara Seas. During the advection of humid air, evaporation decreases and vice versa.

The heat and moist static energy budget indicates that temperature increase in the lower troposphere is almost equally partitioned into turbulent flux, horizontal advection and greenhouse effect. Not only the increased turbulent heat flux over the region of sea ice reduction but also the increased

evaporation plays an important role in Arctic amplification. Specifically, the greenhouse effect produced by the increased specific humidity is comparable in magnitude to that of the increased turbulent heat flux. The increased specific humidity, of course, is a result of moisture source (evaporation minus precipitation) and horizontal advection of moisture as addressed above. Then, the remaining lower tropospheric temperature increase is primarily explained by the horizontal advection of heat. As in the case of moisture budget, the horizontal thermal advection is highly correlated with the lower tropospheric temperature variability. Thus, cold advection results in increased turbulent heat flux and vice versa.

One important caveat in the closure of the heat balance is to quantify the magnitude of the greenhouse effect caused by the increased specific humidity at an arbitrary vertical level. This is accomplished by apportioning the total amount of greenhouse effect in terms of the magnitude of anomalous specific humidity for each level. This obviously is a rough approximation and should eventually be confirmed via a detailed computation using a radiation model.

In conclusion, both the vertical and horizontal processes are needed in explaining the net increase in temperature and specific humidity in association with Arctic amplification. Variability in temperature and specific humidity in the lower troposphere is explained primarily by the horizontal advection of heat and moisture. On the other hand, the vertical source term explains a slightly larger fraction of the mean changes in temperature and specific humidity change than the horizontal advection term. In addition to the role of setting the

“net change” in the lower troposphere, the source terms tend to reduce the magnitude of variability caused by horizontal advection of heat and moisture. That is, sensible and latent fluxes increase (decrease) during the advection of cold and dry (warm and humid) air, thereby partially countering the effect of advection.

A limited test using different reanalysis products indicates that the atmospheric response to the sea ice reduction is generally robust and is not overly sensitive to the choice of reanalysis data. It should be borne in mind, however, that uncertainty is inherent in the quantitative estimates in the present study because of the use of a reanalysis product.

## References

- Årthun, M., Eldevik, T., Smedsrud, L. H., Skagseth, Ø. and Ingvaldsen, R. B. (2012) Quantifying the Influence of Atlantic Heat on Barents Sea Ice Variability and Retreat. *J. Clim.* **25**, 4736-4743.
- Bekryaev, R. V., Polyakov, I. V., and Alexeev, V. A. (2010) Role of Polar Amplification in Long-Term Surface Air Temperature Variation and Modern Arctic warming. *J. Clim.* **23**, 3888-3906.
- Burt, M., Randall, D. and Branson, M. (2016) Dark Warming. *J. Clim.* **29**, 705-719; doi:10.1175/jcli-d-15-0147.1.
- Cavalieri, D. J., Parkinson, C. L. (2012) Arctic sea ice variability and trends, 1979-2010. *The Cryosphere* **6**, 881-889; doi: 10.5194/tc-6-881-2012.
- Cao, Y., Liang, S., Chen, X., He, T., Wang, D. and Cheng, X. (2017) Enhanced wintertime greenhouse effect reinforcing Arctic amplification and initial sea-ice melting. *Sci. Rep.*, **7**, 8462; <https://doi.org/10.1038/s41598-017-08545-2>.
- Chylek, P., Folland, C. K., Lesins, G., Dubey, M. K. and Wang, M. (2009) Arctic air temperature change amplification and the Atlantic multidecadal oscillation. *Geophys. Res. Lett.* **36**, L14801; doi: 10.1029/2009GL038777.
- Cohen, J. et al. (2014) Recent Arctic amplification and extreme midlatitude weather. *Nat. Geosci.* **7**, 627–637.
- Comiso, J. C., Parkinson, C. L., Gersten, R. and Stock, L. (2008) Accelerated decline in the Arctic sea ice cover. *Geophys. Res. Lett.* **35**, L01703; doi:10.1029/2007GL031972.

- Comiso, J. C. (2012) Large Decadal Decline of the Arctic Multiyear Ice Cover. *J. Clim.* **25**, 1176–1193.
- Connolly, R., Connolly, M. and Soon, W. (2017) Re-calibration of Arctic sea ice extent datasets using Arctic surface air temperature records. *Hydro. Sci. J.* **62**(8), 1317-1340; doi: 10.1080/02626667.2017.1324974.
- Dee, D. P. et al. (2011) The ERA-interim reanalysis: Configuration and performance of the data assimilation system. *Q. J. Meteorol. Soc.* **137**, 553-597.
- Deser, C., Walsh, J. E. and Timlin, M. S. (2000) Arctic sea ice variability in the context of recent atmospheric circulation trend. *J. Clim.* **13**, 617-633.
- Deser, C., Tomas, R., Alexander, M. and Lawrence, D. (2010) The Seasonal Atmospheric Response to Projected Arctic Sea Ice Loss in the Late Twenty-First Century. *J. Clim.* **23**, 333-351.
- Francis, J. A. and Hunter, E. (2006) New insight into the disappearing Arctic sea ice. *EOS Trans. Am. Geophys. Union* **87**, 509–511.
- Francis, J. A. and Hunter, E. (2007) Changes in the fabric of the Arctic's greenhouse blanket. *Environ. Res. Lett.* **2**, 045011; doi:10.1088/1748-9326/2/4/045011.
- Graversen, R. G., Mauritsen T., Tjernström, M., Källén, E. and Svensson, G. (2008) Vertical structure of recent Arctic warming. *Nature*, **451**, 53-56.
- Graversen, R. G. and Wang, M. (2009) Polar amplification in a coupled model with locked albedo. *Clim. Dyn.* **33**, 629-643.
- Holland, M. M. and Bitz, C. M. (2003) Polar amplification of climate change in coupled models. *Clim. Dyn.* **21**, 221-232.

- IPCC (2013) Climate Change 2013: The Physical Science Basis (eds Stocker, T. F. et al.). Cambridge Univ. Press, 396-398.
- Iribarne, J. V. and Godson, W. L. (1981) Atmospheric Thermodynamics, 2nd edn. D Reidel Publish.
- Johannessen, O. M., Svetlana, I. K., Leonid, P. B. and Martin, W. M. (2016) Surface air temperature variability and trends in the Arctic: new amplification assessment and regionalization. *Tellus A: Dyn. Met. and Ocean.* **68**; doi: 10.3402/tellusa.v68.28234.
- Kim, B.-M. et al. (2014) Weakening of the stratospheric polar vortex by Arctic sea-ice loss. *Nat. Commun.* **5**, doi:10.1038/ncomms5646.
- Kim, H.-M. and Kim, B.-M. (2017) Relative Contributions of Atmospheric Energy Transport and Sea Ice Loss to the Recent Warm Arctic Winter. *J. Clim.* **30**, 7441–7450; <https://doi.org/10.1175/JCLI-D-17-0157.1>.
- Kim, K. Y., North, G. R. and Huang, J. (1996) EOFs of one-dimensional cyclostationary time series: Computations, examples, and stochastic modeling. *J. Atmos. Sci.* **53**, 1007-1017.
- Kim, K. Y. and North, G. R. (1997) EOFs of harmonizable cyclostationary processes. *J. Atmos. Sci.* **54**, 2416-2427.
- Kim, K. Y., Hamlington, B. D. and Na, H. (2015) Theoretical foundation of cyclostationary EOF analysis for geophysical and climatic variables: Concepts and examples. *Earth-Sci. Rev.* **150**, 201-218.
- Kim, K. Y., Hamlington, B. D., Na, H. and Kim, J. (2016) Mechanism of seasonal Arctic sea ice evolution and Arctic amplification. *The Cryosphere* **10**, 2191-2202; doi:10.5194/tc-10-2191-2016.



- Kim, K. Y. and Son, S. W. (2016) Physical characteristics of Eurasian winter temperature variability. *Environ. Res. Lett.* **11**, 044009.
- Kim, K. Y. (2017) Cyclostationary EOF Analysis: Theory and Applications. Seoul National Univ. Press.
- Koenigk, T. et al. (2013) Arctic climate change in 21st century CMIP5 simulations with EC-Earth. *Clim. Dyn.* **40**, 2719-2743.
- Kumar, A. et al. (2010) Contribution of sea ice loss to Arctic amplification. *Geophys. Res. Lett.* **37**, L21701.
- Kurita, N. (2011) Origin of Arctic water vapor during the icegrowth season. *Geophys. Res. Lett.* **38**; doi:10.1029/2010GL046064.
- Maloney, E. D. (2009) The moist static energy budget of a composite tropical intraseasonal oscillation in a climate model. *J. Clim.* **22**, 711-729.
- Mori, M., Watanabe, M., Shiogama, H., Inoue, J. and Kimoto, M. (2014) Robust Arctic sea-ice influence on the frequent Eurasian cold winters in past decades. *Nat. Geosci.* **7**, 869-873.
- North, G. R. and Erukhimova, T. (2009) Atmospheric Thermodynamics. Cambridge Univ. Press.
- Onarheim, I. H., Eldevik, T., Årthun, M., Ingvaldsen, R. B. and Smedsrud, L. H. (2015) Skillful prediction of Barents Sea ice cover. *Geophys. Res. Lett.* **42**, 5364-5371.
- Overland, J. E., Wood, K. R. and Wang, M. (2011) Warm Arctic-cold continents: climate impacts of the newly open Arctic Sea. *Polar. Res.* **30**, 15787.

- Park, D. S., Lee, S. and Feldstein, S. B. (2015a) Attribution of the recent winter sea ice decline over the Atlantic sector of the Arctic Ocean. *J. Clim.* **28**, 4027-4033.
- Park, H. S., Lee, S., Son, S. W., Feldstein, S. B. and Kosaka, Y. (2015b) The impact of poleward moisture and sensible heat flux on Arctic winter sea ice variability. *J. Clim.* **28**, 5030-5040.
- Petoukhov, V. and Semenov, V. A. (2010) A link between reduced Barents-Kara sea ice and cold winter extremes over northern continents. *J. Geophys. Res.* **115**, D21111.
- Schlichtholz, P. (2011) Influence of oceanic heat variability on sea ice anomalies in the Nordic Seas. *Geophys. Res. Lett.* **38**, L05705; doi:10.1029/2010GL045894.
- Schweiger, A. J., Lindsay, R. W., Vavrus, S., and Francis, J. A. (2008) Relationship between Arctic Sea Ice and Clouds during Autumn. *J. Clim.* **21**, 4799-4810.
- Screen, J. A. and Simmonds, I. (2010a) The central role of diminishing sea ice in recent Arctic temperature amplification. *Nature* **464**, 1334-1337.
- Screen, J. A. and Simmonds, I. (2010b) Increasing fall-winter energy loss from the Arctic Ocean and its role in Arctic amplification. *Geophys. Res. Lett.* **37**, L16707.
- Screen, J. A. et al. (2013) The Atmospheric Response to Three Decades of Observed Arctic Sea Ice Loss. *J. Clim.* **26**, 1230-1248.
- Serreze, M. C. and Francis, J. A. (2006) The Arctic amplification debate. *Clim. Change* **76**, 241-264.

- Serreze, M. C., Holland, M. M., and Stroeve, J. (2007) Perspectives on the Arctic's shrinking sea-ice cover. *Science* **16**, 1533-1536.
- Serreze, M. C., Barrett, A. P., Stroeve, J. C., Kindig, D. N. and Holland, M. M. (2009) The emergence of surface-based Arctic amplification. *The Cryosphere* **3**, 11-19.
- Serreze, M. C. and Barry R. G. (2011) Processes and impacts of Arctic amplification: A research synthesis. *Glob. Planet. Change* **77**, 85-96.
- Serreze, M. C. and Stroeve, J. (2015) Arctic sea ice trends, variability and implications for seasonal ice forecasting. *Philos. Trans. A Math. Phys. Eng. Sci.* **373**, 20140159; <http://dx.doi.org/10.1098/rsta.2014.0159>.
- Smedsrud, L. H. et al. (2013) The role of the Barents Sea in the Arctic climate system. *Rev. Geophys.* **15**, 415-449).
- Spielhagen, R. F. et al. (2011) Enhanced Modern Heat Transfer to the Arctic by Warm Atlantic Water. *Science* **331**, 450-453.
- Tang, Q., Zhang, X., Yang, X. and Francis, J. A. (2013) Cold winter extremes in northern continents linked to Arctic sea ice loss. *Environ. Res. Lett.* **8**, 014036.
- Vihma, T. (2014) Effects of Arctic sea ice decline on weather and climate: a review. *Surv. Geophys.* **35**, 1175-1214.
- Yang, X.-Y., Yuan, X. and Ting, M. (2016) Dynamical link between the Barents-Kara Sea Ice and the Arctic Oscillation. *J. Clim.* **29**, 5103-5122; doi: 10.1175/JCLI-D-15-0669.1.

Yim, B. Y., Min, H. S., Kim, B.-M., Jeong, J.-H. and Kug, J.-S. (2016) Sensitivity of Arctic warming to sea ice concentration. *J. Geophys. Res. Atmos.* **121**, 6927–6942; doi:<https://doi.org/10.1002/2015JD023953>.

## 국문 초록

# 겨울철 북극 증폭에 관한 수직 되먹임 기작과 수평과정과의 상대적 역할 - 바렌츠 카라해를 중심으로 -

김지영

지구환경과학부

서울대학교 대학원

바렌츠-카라해를 중심으로 해빙의 감소가 가속화되고 있으며, 이러한 북극 해빙의 유실 증가를 설명하기 위한 여러가지 메커니즘이 제시되어 왔으나 명확하게 규명이 되지 못하고 있는 실정이다. 본 연구에서는 1일 간격의 ERA Interim 재해석 자료를 이용하여 겨울철 (12월 - 2월) 해빙 감소의 상세한 물리적 메커니즘을 규명하였다. 하향 장파복사가 해빙 감소의 필수 요소이기는 하지만 그 자체만으로는 해빙의 감소를 지속시키지 못하며 해빙이 유실된 해역의 대기에 노출된 해수면에서 과잉 방출되는 열 플럭스에 의해 해빙 감소가 지속될 수 있음을 확인하였다. 증가한 난류 열 플럭스는 하층 대기의 기온과 습도 증가에 기여하며 하향 장파 복사의 증가로 이어진다. 1979년부터 2018년까지의 재해석 자료를 분석한 결과, 이러한 피드백 과정이 바렌츠-카라해를 중심으로 뚜렷하게 나타났으며, 매년 약 8.9%의 비율로 증폭되고 있는 것으로 확인되었다. 과잉 열 플럭스 방출에 의해

지속되는 해빙 감소 피드백 과정은 해빙으로 덮인 다른 극지방에서도 겨울철에 해빙이 완전히 회복되지 않을 경우 유사하게 나타날 수 있을 것으로 예상된다.

한편 열 플러스 방출, 증발 및 강수, 상하향 장파 복사 등과 같은 수직 과정이 해빙 감소에 기여하는 정도를 열과 수증기의 이류에 의한 수평 과정의 기여도와 비교한 상대적인 역할에 대해서도 명확하게 규명이 된 바가 없다. 따라서 본 연구에서는 수평 과정과 수직 과정의 상대적인 역할을 정량적으로 비교하고자 해빙 감소 지역에서의 수분, 열, 습윤 정적 에너지 수지를 분석하였다. 바렌츠-카라 해역 상의 대기 중 기온과 습도의 변화를 설명하기 위해서는 열과 수분의 방출과 같은 수직적 공급원과 이류와 같은 수평적 공급원이 모두 필요한 것으로 나타났으며, 수직 공급원이 평균적으로 기온과 습도 증가에 기여하는 비율이 다소 큰 것으로 계산되었다. 반면, 대기 중의 기온과 습도의 변동성은 수평 이류의 변동성으로부터 기인하는 것으로 확인되었다.

**주요어:** 북극 증폭, 되먹임 기작 (피드백 메커니즘), 수평 및 수직 과정, 바렌츠-카라해, 주기적 정상 경험직교함수

**학 번:** 2012-30893